

# Journal Pre-proof

Mitochondrial AIF loss causes metabolic reprogramming, caspase-independent cell death blockade, embryonic lethality, and perinatal hydrocephalus

Laure Delavallée, Navrita Mathiah, Lauriane Cabon, Aurélien Mazeraud, Marie-Noelle Brunelle-Navas, Leticia K. Lerner, Mariana Tannoury, Alexandre Prola, Raquel Moreno-Loshuertos, Mathieu Baritaud, Laura Vela, Kevin Garbin, Delphine Garnier, Christophe Lemaire, Francina Langa-Vives, Martine Cohen-Salmon, Patricio Fernández-Silva, Fabrice Chrétien, Isabelle Migeotte, Santos A. Susin



PII: S2212-8778(20)30101-0

DOI: <https://doi.org/10.1016/j.molmet.2020.101027>

Reference: MOLMET 101027

To appear in: *Molecular Metabolism*

Received Date: 4 March 2020

Revised Date: 18 May 2020

Accepted Date: 27 May 2020

Please cite this article as: Delavallée L, Mathiah N, Cabon L, Mazeraud A, Brunelle-Navas M-N, Lerner LK, Tannoury M, Prola A, Moreno-Loshuertos R, Baritaud M, Vela L, Garbin K, Garnier D, Lemaire C, Langa-Vives F, Cohen-Salmon M, Fernández-Silva P, Chrétien F, Migeotte I, Susin SA, Mitochondrial AIF loss causes metabolic reprogramming, caspase-independent cell death blockade, embryonic lethality, and perinatal hydrocephalus, *Molecular Metabolism*, <https://doi.org/10.1016/j.molmet.2020.101027>.

This is a PDF file of an article that has undergone enhancements after acceptance, such as the addition of a cover page and metadata, and formatting for readability, but it is not yet the definitive version of record. This version will undergo additional copyediting, typesetting and review before it is published in its final form, but we are providing this version to give early visibility of the article. Please note that, during the production process, errors may be discovered which could affect the content, and all legal disclaimers that apply to the journal pertain.

© 2020 The Author(s). Published by Elsevier GmbH.

# Mitochondrial AIF loss causes metabolic reprogramming, caspase-independent cell death blockade, embryonic lethality, and perinatal hydrocephalus

Laure Delavallée<sup>1</sup>, Navrita Mathiah<sup>2#</sup>, Lauriane Cabon<sup>1#</sup>, Aurélien Mazeraud<sup>3#</sup>, Marie-Noelle Brunelle-Navas<sup>1</sup>, Leticia K. Lerner<sup>1</sup>, Mariana Tannoury<sup>1</sup>, Alexandre Prola<sup>4,5</sup>, Raquel Moreno-Loshuertos<sup>6</sup>, Mathieu Baritaud<sup>1</sup>, Laura Vela<sup>1</sup>, Kevin Garbin<sup>7</sup>, Delphine Garnier<sup>1</sup>, Christophe Lemaire<sup>4</sup>, Francina Langa-Vives<sup>8</sup>, Martine Cohen-Salmon<sup>9</sup>, Patricio Fernández-Silva<sup>6</sup>, Fabrice Chrétien<sup>3</sup>, Isabelle Migeotte<sup>2</sup>, and Santos A. Susin<sup>1\*</sup>

<sup>1</sup> Centre de Recherche des Cordeliers, Cell Death and Drug Resistance in Hematological Disorders Team, INSERM UMRS\_1138, Sorbonne Université, USPC, Université Paris Descartes, Université Paris Diderot, Paris, France

<sup>2</sup> Institut de Recherche Interdisciplinaire en Biologie Humaine et Moléculaire, Université Libre de Bruxelles, Brussels, Belgium.

<sup>3</sup> Experimental Neuropathology Unit, Institut Pasteur, Paris, France. Université Paris Descartes, Sorbonne Paris Cité, Paris, France. Neuropathology Service, Sainte-Anne Hospital Center, Paris, France.

<sup>4</sup> INSERM UMRS 1180, LabEx LERMIT, Châtenay-Malabry, France. Faculté de Pharmacie, Université Paris-Sud, Châtenay-Malabry, France. Université de Versailles Saint Quentin en Yvelines, Versailles, France.

<sup>5</sup> U955-IMRB Team 10 BNMS, INSERM, UPEC, Université Paris-Est, Ecole Nationale Vétérinaire de Maisons-Alfort, France

<sup>6</sup> Departamento de Bioquímica, Biología Molecular y Celular, Universidad de Zaragoza, Zaragoza Spain. Instituto de Investigación en Biocomputación y Física de Sistemas Complejos (BiFi), Universidad de Zaragoza, Zaragoza Spain.

<sup>7</sup> Centre de Recherche des Cordeliers, Genotyping and Biochemical facility, INSERM UMRS\_1138, Sorbonne Université, USPC, Université Paris Descartes, Université Paris Diderot, Paris, France

<sup>8</sup> Centre d'Ingénierie Génétique Murine, Institut Pasteur, Paris, France.

<sup>9</sup> Physiology and Physiopathology of the Gliovascular Unit, Collège de France-Center for Interdisciplinary Research in Biology (CIRB)/CNRS UMR 7241/INSERM U1050/Sorbonne Université, Paris, France.

**Running title: AIF controls mouse development and cell fate**

# N. Mathiah, L. Cabon, and A. Mazeraud contributed equally to this work

\* **Corresponding author:** Dr. Santos A. Susin. Centre de Recherche des Cordeliers, 15, rue de l'École de Médecine, 75006 Paris, France. Phone: +33144279070; Fax: +33144279036; E-mail: santos.susin@sorbonne-universite.fr

## Highlights

Mitochondrial AIF loss triggers OXPHOS/metabolism impairment

*AIF*<sup>-Y</sup> MEFs reprogram their metabolism by enabling an AMPK/GLUT-4 glycolytic pathway

The OXPHOS dysfunction associated to AIF loss generates a P53/P21 senescent phenotype

The lack of metabolic plasticity provokes embryonic lethality in the AIF KO animals

*AIF*<sup>+/-</sup> females develop immune cell exhaustion and perinatal hydrocephaly

## Objectives

Apoptosis-Inducing Factor (AIF) is a protein involved in mitochondrial electron transport chain assembly/stability and in programmed cell death. The relevant role of this protein is underlined by the fact that mutations altering mitochondrial AIF properties result in acute pediatric mitochondrialopathies and tumor metastasis. By generating an original AIF-deficient mouse strain, the present study sought to analyze, in a single paradigm, the cellular and developmental metabolic consequences of AIF loss and the subsequent oxidative phosphorylation (OXPHOS) dysfunction.

## Methods

We developed a novel AIF-deficient mouse strain and assessed, by molecular and cell biology approaches, the cellular, embryonic, and adult mice phenotypic alterations. Additionally, we carried out *ex vivo* assays with primary and immortalized AIF knockout mouse embryonic fibroblasts (MEFs) to establish the cell death characteristics and the metabolic adaptive responses provoked by the mitochondrial electron transport chain (ETC) breakdown.

## Results

AIF deficiency destabilized mitochondrial ETC and provoked supercomplex disorganization, mitochondrial transmembrane potential loss, and high generation of mitochondrial reactive oxygen species (ROS). *AIF<sup>-Y</sup>* MEFs counterbalanced these OXPHOS alterations by mitochondrial network reorganization and a metabolic reprogramming towards anaerobic glycolysis illustrated by the AMPK phosphorylation at Thr172, the overexpression of the glucose assimilation transporter GLUT-4, the subsequent enhancement of glucose uptake, and the anaerobic lactate generation. A late phenotype was characterized by the activation of P53/P21-mediated senescence. Interestingly, about 2% of *AIF<sup>-Y</sup>* MEFs diminished both mitochondrial mass and ROS levels and spontaneously proliferated. These cycling *AIF<sup>-Y</sup>* MEFs were resistant to caspase-independent cell death inducers. The AIF-deficient mouse strain was embryonic lethal between E11.5 and E13.5 with energy loss, proliferation arrest, and increased apoptotic levels. Contrary to *AIF<sup>-Y</sup>* MEFs, the AIF KO embryos were unable to reprogram their metabolism towards anaerobic glycolysis. Heterozygous *AIF<sup>+/-</sup>* females displayed a progressive bone marrow, thymus, and spleen cellular loss. In addition, about 10% of *AIF<sup>+/-</sup>* females developed perinatal hydrocephaly characterized by brain development impairment, meningeal fibrosis, and medullar hemorrhages; those mice died around 5 weeks of age. *AIF<sup>+/-</sup>* with hydrocephaly exhibited loss of ciliated epithelium in the ependymal layer. This phenotype seemed triggered by the ROS excess. Accordingly, it was possible to diminish the occurrence of hydrocephalus *AIF<sup>+/-</sup>* females by supplying dams and newborns with an antioxidant in drinking water.

## Conclusion

In a single knockout model and at three different levels (cell, embryo, and adult mice) we demonstrated that, by controlling the mitochondrial OXPHOS/metabolism, AIF is a key factor regulating cell differentiation and fate. Additionally, by shedding new light on the pathological consequences of mitochondrial OXPHOS dysfunction, our new findings pave the way for novel pharmacological strategies.

## KEYWORDS

AIF / Caspase-independent cell death / Hydrocephaly / Metabolism / Mitochondria / OXPHOS

## ABBREVIATIONS

2-Deoxyglucose (2-DG); 2-[*N*-(7-nitrobenz-2-oxa-1,3-diazol-4-yl) amino]-2-deoxy-d-glucose (2-NBDG); Apoptosis-inducing factor (AIF); 5' adenosine monophosphate-activated protein kinase (AMPK); Blue native polyacrylamide gel electrophoresis (BN-PAGE); Bromodeoxyuridine (BrDU); Cerebrospinal fluid (CSF); Cyclin-dependent kinase inhibitor 1A (CDKN1 $\alpha$ ; P21); Cyclooxygenase (COX); Dynamin-related protein 1 (DNM1L; DRP1); Electron transfer chain (ETC); Fluoro-carbonyl cyanide phenylhydrazone (FCCP); Glucose transporter 1 (GLUT-1); Glucose transporter 1 (GLUT-4); Harlequin (Hq); Hematopoietic stem cells (HSC); Hydrocephalus (HC); Knockout (KO); Mean fluorescence intensity (MFI); Mitochondrial dynamin like GTPase (OPA1); Mitochondrial fission 1 protein (FIS1); Mitochondrial fission factor (MFF); Mitofusin 1 (MFN1); Mitofusin 2 (MFN2); Mouse embryonic fibroblasts (MEFs); *N*-Methyl-*N'*-nitro-*N*-nitrosoguanidine (MNNG); *N,N,N',N'*-tetramethyl-*p*-phenylenediamine, (TMPD); Oxidative phosphorylation (OXPHOS); Paraformaldehyde (PFA); Paternal X chromosome (Xp); Phosphatidylserine (PS); Programmed cell death (PCD); Propidium iodide (PI); Reactive oxygen species (ROS); Retinoblastoma protein (pRb); Staurosporine (STS); Succinate dehydrogenase (SDH); Supercomplex (SC); Superoxide dismutase 1 (SOD1); Superoxide dismutase 2 (SOD2); Wild-type (WT).

Mitochondria are wide-ranging organelles that, via oxidative phosphorylation (OXPHOS), play a key role in the cell by providing energy in the form of ATP and by generating the reactive oxygen species (ROS), which regulate differentiation and fate [1-6]. During OXPHOS, fuel substrates are oxidized and electrons transferred through the mitochondrial electron transfer chain (ETC), a branched chain of multi-protein complexes (complex I to IV). This process is chemiosmotically coupled to the phosphorylation of ADP to ATP by the ATP synthase (complex V). Mitochondrial ROS arise from the 0.1-2% of electrons that escape from the ETC [7]. Currently, the more accepted model of ETC organization is the so-called “plasticity model”, which proposes different stable interactions between complexes (such as I and III, or I, III and IV) in entities named mitochondrial supercomplexes (SCs) [8; 9].

AIF is a bi-functional protein, encoded by *Aifm1* (*Pdcd8*) on the X-chromosome, implicated in maintaining a functional mitochondrial OXPHOS and, after its translocation to the nucleus, in programmed cell death (PCD) [10-24]. The role of AIF in mitochondrial complexes assembly seems to relate to its interaction with CHCHD4, a component of the mitochondrial protein import machinery [12; 13]. In this way, AIF or CHCHD4 mutations are concomitant with OXPHOS deficiency-related mitochondrialopathies (encephalopathy, infantile motor neuron disease, and early prenatal ventriculomegaly) [25-28]. Moreover, it seems that the mitochondrial role of AIF is critical for inhibiting tumor metastasis [29] and that AIF overexpression aggravates hypoxic-ischemic brain injury in neonatal mice [30].

AIF role has been mainly assessed in the hypomorphic Harlequin (Hq) mice strain, which is not an AIF KO mouse but presents about 70 % ubiquitous reduction in AIF expression [10]. Among others, the Hq strain exhibits T-cell development defaults, chronic neurodegeneration, progressive cerebellar ataxia, Purkinje cell degeneration, optic tract dysfunction, early fur abnormalities, and hypertrophic cardiomyopathy [10; 16; 17; 31-33]. Studies on AIF have been complemented by the characterization of tissue-specific knockout models that corroborated T-cell developmental alterations, delayed neurogenesis, skeletal muscle atrophy, and dilated cardiomyopathy [14; 15; 34]. Finally, in a novel mouse model in which *Aifm1* was ablated early during hematopoiesis, we observed hematopoietic stem cells (HSC) loss, thymopoiesis blockade, and delayed development of the T-cell, B-cell, and erythroid lineages [35; 36].

Here, by generating a *bona fide* AIF KO mouse strain, we illustrate in a single model the consequences of the mitochondrial OXPHOS dysfunction associated with the loss of AIF at cellular, embryonic, and adult mice levels. The generation of veritable AIF KO mice uncovers new metabolic and phenotypic adaptive responses, reveals a greater role for AIF and mitochondrial OXPHOS in mouse development, and clarifies the AIF function in caspase-independent PCD.

### 2.1 Mice

Mice were housed at the Cordeliers Center animal facility under strictly controlled, specific-pathogen-free conditions (agreement B75-06-12). Experiments were performed in accordance with ARRIVE ethical guidelines and with the approval of the French Ministry of Agriculture (agreement 1675). Animals were maintained with a rodent diet (R03, Scientific Animal Food & Engineering Diets) and water was made available *ad libitum* in a vivarium with a 12-h light-dark cycle at 22° C. In specific experiments, dams and newborns were fed a high fat ketogenic diet (HFD; Research Diets) supplied or not with riboflavin (5mg/100 mL) in drinking water.

*Aifm1* floxed mice were generated by flanking the exon 11 of *Aifm1* with LoxP sequences using standard gene-targeting techniques (Genoway, France). After fifteen backcrosses into the C57BL/6J background, *Aifm1* floxed males (*Aifm1<sup>fl/Y</sup>*; *AIF<sup>fl/Y</sup>*) were crossed to PGK-Cre females (kindly provided by Yvan Lallemand, Pasteur Institute). This crossing induced an excision of exon 11 in *Aifm1* that resulted in a frameshift mutation and the creation of a stop codon in exon 12. The resulting *Aifm1<sup>+/-</sup>* (*AIF<sup>+/-</sup>*) females were identified by genomic PCR assessment (see Supplemental Fig. 1C). For hematological analysis, females were euthanized at 6 months old. Spleens, lymph nodes, thymus, and bone marrow were sampled in order to prepare single cell suspensions by mechanical disruption and passage through a cell strainer. Absolute cell counts were then assessed.

In embryo studies, *AIF<sup>+/-</sup>* females were crossed with *Aifm1<sup>+/Y</sup>* (*AIF<sup>+/Y</sup>*) males. E7.5 to E13.5 embryos were dissected with the help of a stereomicroscope (M80; Leica) and pictures were obtained with an IC80 HD camera (Leica).

### 2.2 Generation of *AIF<sup>-/Y</sup>* mouse embryonic fibroblasts (MEFs)

To generate *AIF<sup>-/Y</sup>* MEFs, *AIF<sup>fl/Y</sup>* females were crossed to *Rosa26-CreERT2* males (provided by Dr. Anton Bernes, NCI, Amsterdam, The Netherlands) [37] and MEFs were generated from triple E12.5 transgenic male embryo. To obtain *AIF<sup>-/Y</sup>* cells, MEFs were treated overnight with tamoxifen (4-OHT; 1  $\mu$ M).

### 2.3 Southern blot

Genomic DNA from WT (Co) and AIF-deficient (*AIF<sup>-/Y</sup>*) MEFs (4 days post-treatment with tamoxifen; 4-OHT) was extracted using Wizard Genomic DNA purification kit (Promega) and digested with Pci1. Obtained genomic DNA fragments, including those encompassing exons 7 to 13 of *Aifm1*, were separated on a 0.8% agarose gel and transferred to hybond membrane. Membrane was baked 2 h at 80°C to fix DNA, then hybridized with a probe labeled with Gene Images

AlkPhos direct labeling and detection system kit from GE Healthcare. The probe, specific to the 3'end of AIF genomic DNA, was freshly prepared by PCR amplification of genomic DNA using sense (intron 12 nucleotides 33070-33098) and reverse (intron 13 nucleotides 33433-33459) primers. Membrane was then washed, and the hybridization pattern revealed using CDP star (Amersham). Images were acquired on a MF-ChemiBIS 4.2 (DNR Bio-Imaging Systems).

## 2.4 Mitochondrial and cellular analysis

For mitochondrial ROS, mitochondrial mass, and  $\Delta\Psi_m$  measurements, MEFs were incubated with MitoSOX (5 $\mu$ M), Mitotracker Green (100 nM), or Mitotracker Red (100 nM) (ThermoFisher Scientific) respectively before assessment in a FACSCanto II (BD Biosciences) in the total population (10,000 cells). Data were analyzed using FlowJo software and were expressed as MFI (mean fluorescence intensity), which referred to the fluorescence intensity of each event on average. Additionally, lysed 15 x 10<sup>3</sup> WT and *AIF*<sup>-/-</sup> MEFs or 1 x 10<sup>4</sup> cells from embryos dissociated in trypsin were tested for ATP content with a luciferin-luciferase kit (Abcam) and expressed as ATP/ADP ratio or RLU (relative light units). In some experiments, MEFs were pre-treated with oligomycin (10  $\mu$ M) before ATP assessment. Measures were performed in an Infinite M100 PRO plate reader (Tecan).

To analyze glucose assimilation, MEFs were incubated (30 min; 37°C) in glucose-free DMEM with 2-NBDG (100  $\mu$ M; ThermoFisher Scientific) prior to flow cytometry assessment in the total population (10,000 cells).

Glycolytic and GLUT-4 dependency was verified in MEFs treated or not with indinavir (50  $\mu$ M; Selleckchem) or 2-Deoxy-D-Glucose (2-DG; 10 mM); AMPK dependency was verified in MEFs pretreated or not with dorsomorphin (Compound C; 25  $\mu$ M; Selleckchem); the induced cell death rate was assessed by an Annexin-V-APC (0.1  $\mu$ g/ml; BD Biosciences) and propidium iodide double labeling on a FACSCanto II in the total population (10,000 cells).

In cell cycle analyses, MEFs were incubated (30 min; 37°C) with BrdU (10 $\mu$ M). After fixation and partial DNA denaturation, cells were co-stained with an anti-BrdU-FITC antibody (25  $\mu$ g/mL; BD Biosciences) and propidium iodide prior to flow cytometric measurement in the total population (10,000 cells).

Senescence was recorded in MEFs treated with chloroquine diphosphate (300  $\mu$ M, 2 h) to induce lysosomal alkalinisation. Then, C<sub>12</sub>FDG (Thermofisher Scientific) was added at 33  $\mu$ M during 2 h and cells were washed twice with PBS before performing the cytofluorometric quantification.

Cell death was assessed by flow cytometry in the total population (10,000 cells) using Annexin-V-APC (assessment of phosphatidylserine exposure; 0.1  $\mu$ g/ml) and propidium iodide (cell viability)



co-labeling. In some experiments, WT and *AIF*<sup>-/-</sup> MEFs were pretreated during 30 min with MNNG (250  $\mu$ M, 9 h), staurosporine (STS; 1  $\mu$ M, 6 h),  $\beta$ -Lapachone (4  $\mu$ M; 18 h), or etoposide (20  $\mu$ M, 6 h) before flow cytometry assessment of cell death. In caspase-dependent control experiments, MEFs were pretreated during 30 minutes with QVD.OPh (1  $\mu$ M) before etoposide treatment.

For lactate measurement in MEFs, cells were cultured for 2 h in a serum-free medium and centrifuged. The amounts of lactate in the supernatants were quantified in the Infinite M100 PRO plate reader using the L-lactate kit from Cayman Chemical. Lactate was also quantified in embryos dissociated in 50  $\mu$ L of the L-lactate kit assay buffer. After centrifugation, the quantity of lactate in 10  $\mu$ L of the supernatant was assessed.

## 2.5 Clark electrode

Oxygen consumption was measured in  $5 \times 10^6$  WT and *AIF*<sup>-/-</sup> MEFs as previously described [38]. In non-permeabilized cells, respiration was measured under basal conditions in DMEM medium and in response to the sequential addition of oligomycin (10  $\mu$ M), fluoro-carbonyl cyanide phenylhydrazone (FCCP; 5  $\mu$ M), amytal (2 mM), and azide (5 mM). In digitonin-permeabilized cells (1  $\mu$ g/ $\mu$ L, 5 min), respiration was measured in response to the sequential addition of glutamate/malate (10 mM/4 mM), ADP (2 mM), Amytal (2 mM), Succinate (10 mM), Malonate (10 mM), Glycerol-3-Phosphate (15 mM), Myxothiazol (0.5  $\mu$ M), Tetramethyl-phenylenediamine (TMPD)/ascorbate (0.5 mM/2mM) and Azide (5 mM).

## 2.6 Mitochondrial supercomplex (SC) assessment

Mitochondria were purified from control (0) or 4-OHT-treated MEFs (4 to 16 days post-treatment) and permeabilized by digitonin. Solubilized complexes and supercomplexes were separated by 1D BN-PAGE and revealed by the NADH dehydrogenase in-gel activity (0.1 mg/ml NADH and 2.5 mg/ml Nitrotetrazolium Blue chloride). Alternatively, the mitochondrial complexes I, III, IV, and SCs were visualized by immunoblot using antibodies against NDUFA9 (20C11B11B11, Life technologies), UQCRC2 (13G12AF12BB11, Abcam), or COX4I2 (20E8C12, Abcam). Immunoreactive proteins were detected using HRP-conjugated secondary antibodies and visualized with the ECL chemiluminescence kit (Thermo Scientific). Images were acquired using the MF-ChemiBIS 4.2 imager.

## 2.7 Immunofluorescence

MEFs seeded on coverslips were fixed in paraformaldehyde (PFA; 2%) and incubated with the mitochondrial marker Mitotracker Red (20 nM; Thermo Fisher) and the nuclear dye Hoechst 33342. Slides were imaged using a LSM 710 Zeiss confocal microscope and analyzed using the image J software.

## 2.8 Electron microscopy

Control (D0) or tamoxifen-treated MEFs (12 to 16 days post-treatment) were fixed at 4° C for 2 h in 2.5 % glutaraldehyde in 0.1 M phosphate buffer (pH 7.3), postfixed for 1 h in 1 % buffered osmium tetroxide, dehydrated through a graded ethanol series, and embedded in Epon 812. The ultrathin sections were counterstained with 2% aqueous uranyl acetate for 30 min, then with lead citrate for 10 min and finally viewed under a Philips 100X electron microscope. Alternatively, freshly dissected E9.5 WT and *AIF*<sup>-Y</sup> embryos were fixed, processed for ultrathin sections, counterstained, and examined as above.

## 2.9 Lentiviral transduction

An in-frame c-terminal tag encoding the V5 epitope was first added to the AIF-wt cDNA (plasmid pcDNA3.1 mAIFV5). The resulting cDNA was then subcloned into the pLVX-IRES-Zs-Green lentiviral vector (Clontech-Takara Bio Europe, Saint-Germain-en-Laye, France). Viruses were produced into 293T cells by CaCl<sub>2</sub> transient transfection of the lentiviral constructs and the packaging plasmids pCMV-VSV-G and pCMV-dR8.2 dvpr (Addgene plasmids 8454 and 8455, respectively) [39]. Forty-eight hours after transfection, lentiviral supernatants were harvested, clarified by filtration, and used immediately for *AIF*<sup>-Y</sup> MEFs transduction with 6 µg/ml of polybrene. Seventy-two hours after transduction, GFP positive cells were sorted, expanded, and AIF location and mitochondrial network distribution visualized by immunofluorescence as above.

## 2.10 Immunoblotting

MEFs or freshly dissected embryos were lysed in buffer containing 50 mM Tris pH 7.5, 150 mM NaCl, 1 mM EDTA, 1% Triton X-100, and the protease/phosphatase inhibitor cocktail from Roche. Protein concentration was determined using the BioRad Protein Assay. Equal amounts of total proteins (50 µg) were loaded on linear SDS-PAGE gels and transferred onto a PVDF or nitrocellulose membrane. Membrane blocking and antibody incubations were performed in TBS 0.1% Tween 20 plus 5% non-fat dry milk. The primary antibodies used were: AIF (D-20, Santa Cruz), NDUFA9 (20C11B11B11, Life technologies), NDUFS3 (3F9DD2, Life technologies), SDHA (2E3GC12FB2AE2, Life technologies), UQCRC2 (13G12AF12BB11, Abcam), COX1 (35-8100; Thermo Fisher), COX4I2 (20E8C12, Abcam), ATP5B (3D5AB1, Life technologies), AMPKalpha (Cell signaling) and phospho-AMPKalpha (Thr172, Cell signaling), p21Cip1 (C-19, Santa Cruz), Phospho-Rb (Cell Signaling), and β-Actin (AC15, Sigma). Immunoreactive proteins were detected using HRP-conjugated secondary antibodies and visualized with SuperSignal West Dura chemiluminescence kits (Thermo Scientific). Immunoblot images were acquired in the MF-ChemiBIS 4.2 imager.

Brains from WT,  $AIF^{-/X}$ , and  $AIF^{-/X}$  HC females dissected and frozen in liquid nitrogen were used for protein carbonyls detection. After generation of brain homogenates (2 mg), biotin-hydrazide (60 mM), sodium cyanoborohydride (30 mM), and trichloroacetic acid (10 %) were successively added to the samples. After centrifugation, pellets were washed with 1:1 ethanol/ethyl acetate and dissolved in Laemmli buffer. Then, equal amounts of total proteins (50  $\mu$ g) were loaded on linear SDS-PAGE gels and transferred onto a PVDF membrane. Protein carbonyls were visualized, using streptavidin-HRP, revealed by chemiluminescence, and quantified using the Multi Gauge 3.0 software (Fujifilm Life Sciences). The optical density was normalized according to an endogenous background and was expressed relative to the data obtained in untreated cells (= 1.0).

## 2.11 Quantitative RT-PCR

Total RNA from cells, embryos or brain was extracted using the Nucleospin® RNA II kit (Macherey-Nagel). cDNA was prepared using Superscript® II reverse transcriptase (Life Technologies). Quantitative RT-PCR was performed using the TaqMan® Gene Expression Assays (Life Technologies) for *Mfn1* (mitofusin 1), *Mfn2* (mitofusin 2), *Opal* (mitochondrial dynamin like GTPase); *Fis1* (mitochondrial fission 1 protein); *Dnm1l* (dynamin-related protein 1); *Mff* (mitochondrial fission factor); *Sod1* (Super oxide dismutase 1), *Sod2* (Super oxide dismutase 2), *Glut-1* (*Slc2a1*, solute carrier family 2 (facilitated glucose transporter), member 1), *Glut-4* (*Slc2a4*, solute carrier family 2 (facilitated glucose transporter), member 4), *Tp53* (tumor protein p53), *Cdkn1 $\alpha$*  (cyclin-dependent kinase inhibitor 1A; P21), or *Pgc1 $\alpha$*  (Peroxisome proliferator-activated receptor gamma coactivator 1-alpha). PCR reactions were performed in triplicate using TaqMan® Fast advanced Master Mix (Life Technologies). The products were amplified in a ViiA7 Real-time PCR System (Life Technologies) at 60°C for 40 cycles. Data were evaluated using the comparative threshold cycle method. The housekeeping expression of *18S* was utilized to normalize the data.

## 2.12 Histology

We developed a specific method of embedding without prior macroscopic dissection of the brain in order to be able to observe both neural tissue with brain envelope and the skull bone on the same histology slide. Wild-type (WT) and  $AIF^{-/X}$  hydrocephalus (HC) females were fixed by perfusion in 4% PFA. After decalcification with 0.1 N nitric acid and paraffin embedding, 4  $\mu$ m thick sections were stained with hematoxylin-eosin. Some tissues were processed without paraffin embedding before vibratome sectioning (for 100  $\mu$ m thick floating sections). E9.5 WT and  $AIF^{-/Y}$  embryos were fixed in 4% PFA, embedded in acrylic resin (historesin acrylic® Leica) before 3  $\mu$ m sectioning and hematoxylin-eosin staining. Images were obtained using a Leica photomicroscope.

### 2.13 Immunohistochemistry

Brains of WT and *AIF*<sup>+/-</sup> HC females were fixed in PFA (4 %). After decalcification, free-floating brain sections (100  $\mu$ m) were fixed in PFA before performing the immunostaining with anti-Iba1 (1:100e Dako). We used a long incubation process (24 h) after deterging the lipid with high concentration triton X (1%). Nuclei were counterstained with the nuclear dye Hoechst 33342. Slides were imaged using a LSM 710 Zeiss confocal microscope and analyzed using the image J software.

The activities of Cyclooxygenase (COX) and succinate dehydrogenase (SDH) were visualized to explore respiratory dysfunction in embryos [40]. Briefly, E9.5 WT and *AIF*<sup>-Y</sup> embryos were dissected, placed in plastic mold containing cold optimal cutting temperature (OCT) compound and snap-frozen in nitrogen liquid. 14  $\mu$ m cryosections, obtained using cryostat CM 3050S (Leica), were incubated for 40 min at 37 °C with 3,3'-diaminobenzidine tetra-hydrochloride, 500  $\mu$ M cytochrome c, and bovine catalase. The sections were then washed four times at 10 min in 0.1 M PBS (pH 7.0). Next, 1.875 mM nitroblue tetrazolium (NBT), 1.30 M sodium succinate, 2.0 mM phenazine methosulfate (PMS), and 100 mM sodium azide were applied for 40 min at 37 °C. Sections were finally washed, cover-slipped, and visualized under bright field microscopy.

To evaluate proliferation in embryo, pregnant females were intraperitoneally injected with BrdU (0.1mg BrdU/g of body weight) one hour before embryonic dissection. E8.5 and E9.5 WT and *AIF*<sup>-Y</sup> embryos were identified by PCR, dissected, and kept in separated well plates in ice cold PBS/BSA 0.4 %. After fixation in ice-cold EtOH (70 %; H<sub>2</sub>O) overnight, embryos were rehydrated with ice cold EtOH 50 % during fifteen minutes at 4°C, then washed with ice cold PBS/BSA 0.4%. Embryos were then submerged in sucrose 30% (diluted in phosphate buffer 0.1 M, pH 7.4) until they reached the bottom of the well. Then, embryos were placed in molds containing cold OCT and snap-frozen in liquid nitrogen. Further, 10-12  $\mu$ m cryosections were made using the cryostat CM 3050S and processed for BrdU immunostaining. Briefly, sections were quenched with H<sub>2</sub>O<sub>2</sub> 0.6 % and MetOH 1 % in PBS for 1h at RT. After washing, slides were unmasked with HCl 3.7 % and processed with sodium borate 0.1 M. After a pre-blocking step, an anti-BrdU antibody (BD Biosciences) was added on top of each section and a secondary biotinylated antibody was added. Slides were next incubated with streptavidin-488 and Hoechst. Images were obtained on a fluorescent microscope Axiovert 200M (Zeiss).

For embryonic cell death detection, E8.5 and E9.5 WT and *AIF*<sup>-Y</sup> embryos were dissected, fixed in PFA (4 %), embedded in cold OCT and snap-frozen in liquid nitrogen. 10-12  $\mu$ m cryosections, made with the cryostat CM 3050S, were fixed in methanol/acetic acid solution (2:1) at -20°C. After permeabilization, TUNEL mix (Roche Diagnostics) was added on top of each section for one hour

at 37°C. After two washing steps, nuclei were colored by Hoechst 33342. Images were obtained on a fluorescent microscope Axiovert 200M (Zeiss) using transmitted light.

#### **2.14 Statistics**

Results, displayed as mean  $\pm$  SEM, were statistically analyzed by the Mann-Whitney or student *t*-tests using the GraphPad Prism software. Significant *p* values were indicated as follows: \*  $p \leq 0.05$ , \*\*  $p \leq 0.01$ , \*\*\*  $p \leq 0.001$ . All the experiments were independently repeated at least three times.

Chemicals and reagents were purchased from Sigma-Aldrich except where otherwise noted.

Journal Pre-proof

### 3. RESULTS

#### 3.1 $AIF^{-/Y}$ MEFs were OXPHOS defective and showed extensive ETC supercomplex disorganization.

To analyze mitochondrial and cellular alterations associated with AIF loss, we generated a primary mouse embryonic fibroblasts knockout (KO) for AIF ( $AIF^{-/Y}$  MEFs) by crossing Rosa26-CreERT2 mice [37] with our novel *Aifm1* floxed strain (Figure 1A and Supplemental Fig. 1). Tamoxifen (4-OHT) treatment of  $AIF^{F/Y}$ ; RosaCre ERT2<sup>+/-</sup> MEFs provoked progressive AIF protein loss (Figure 1B), which destabilized mitochondrial ETC complexes I and IV (e.g. loss of NDUFA9, NDUFS3 and COX4I2 proteins). Complexes II, III and V (ATP synthase) remained unaltered (Figure 1B). Complementary blue native polyacrylamide gel electrophoresis (BN-PAGE) and immunoblot assessments revealed that AIF deficiency, in addition to a strong reduction in free complex I levels, also provoked ETC SC disorganization with a rapid loss of complex I<sub>2</sub> + complex III<sub>2</sub> and triple complex I + complex III<sub>2</sub> + complex IV structures and a more delayed disruption of complex I + complex III<sub>2</sub> organization (Figure 1C). These observations are in accordance with the “plasticity” model of ETC structure in which the alteration of individual complexes directly affects the supercomplex organization [8; 9; 41].

Analysis of the oxygen consumption rate confirmed that mitochondrial respiration was significantly altered in  $AIF^{-/Y}$  MEFs. As described in Supplemental Fig. 2A, compared to control MEFs (cells before 4-OHT treatment; D0),  $AIF^{-/Y}$  MEFs (16 days post-tamoxifen treatment; D16) exhibited significant reduction of oxygen consumption in both phosphorylating (basal) and non-phosphorylating (+ oligomycin) conditions. The total oxidative capacity, assessed by the presence of the ionophore FCCP, was also compromised in KO cells. Treatment with the complex I inhibitor amytal abolished the remaining oxygen consumption of  $AIF^{-/Y}$  MEFs, indicating that complex I remained slightly functional. Finally, analysis of the individual complex activities revealed that complexes I to IV activities were affected by AIF deficiency (Supplemental Fig. 2B).

Mitochondrial labeling revealed that the kinetic of AIF disappearance was linked to the progressive disruption of the mitochondrial network (Figure 1D, upper panels). Remarkably, at D12 post-tamoxifen, electronic microscopy pictures uncovered elongated mitochondria, suggesting a mitochondrial fusion development (Figure 1D, lower panels). This is substantiated by the quantitative RT-PCR analysis of central executioners of mitochondrial dynamics. Indeed, as depicted in Figure 1E, in contrast to the fission factors FIS1, DNM1L (DRP1) and MFF, the mRNA of the key members of the fusion machinery MFN1, MFN2, and OPA1 appeared significantly overexpressed in the  $AIF^{-/Y}$  MEFs at D12 post-tamoxifen treatment. Thus, although the inhibition of the mitochondrial fission machinery could also contribute to the elongated mitochondrial phenotype observed in the  $AIF^{-/Y}$  MEFs at D12 post-tamoxifen treatment, our multiparametric assessment

points toward the prevalence of a transient mitochondrial fusion process. Further, upon complete AIF disappearance (D16 post-tamoxifen treatment), we observed a highly fragmented mitochondrial network associated to cellular vacuolization (Figure 1D). These alterations provoked a significant diminution in the cellular mitochondrial transmembrane potential and a high generation of mitochondrial ROS (Figures 1F and G). The excess of ROS triggered mRNA overexpression of mitochondrial SOD2 (Superoxide dismutase 2), a protein that partially regulated the excess of superoxide OXPHOS products (Figure 1H). Surprisingly, despite mitochondrial dysfunction, ATP levels were relatively preserved in *AIF*<sup>-Y</sup> MEFs (Figure 1I). One possible explanation would be that MEFs normally generate ATP by non-mitochondrial pathways. Alternatively, it is possible that AIF KO MEFs have reprogrammed their metabolism to counterbalance mitochondrial OXPHOS dysfunction. To evaluate this dichotomy, we treated control and *AIF*<sup>-Y</sup> MEFs with oligomycin, which specifically blocks the mitochondrial ATP synthase and, thus, inhibits the generation of mitochondrial ATP. In control MEFs, oligomycin treatment dramatically diminished ATP levels, indicating that these cells generate most of the ATP via mitochondria. In contrast, oligomycin marginally modified ATP levels in *AIF*<sup>-Y</sup> MEFs, suggesting that these cells generate ATP via a non-mitochondrial pathway (Figure 1I). Those results suggest that *AIF*<sup>-Y</sup> MEFs were able to modify their metabolism to compensate for mitochondrial OXPHOS dysfunction.

**The OXPHOS damage associated with AIF deficiency was counterbalanced by a shift towards anaerobic glycolysis and the development of a senescent phenotype.**

Following our above results, we sought to analyze the mechanism associated to the adaptive metabolic features of *AIF*<sup>-Y</sup> MEFs. More precisely, by measuring the phosphorylation of AMPK at Thr172 and the mRNA expression of the main glucose transporters expressed in fetal tissues and fibroblasts (GLUT-1 and GLUT-4), we first assessed whether the AIF loss was accompanied by a modification in the glucose assimilation pathway. Phosphorylation of AMPK, a central regulator of energy homeostasis, is a point of convergence of metabolic and genomic stress signals [42-45]. Indeed, AMPK is a major energy-sensing kinase that plays a role in cellular energy homeostasis by activating a whole variety of catabolic processes in multicellular organisms, such as glucose uptake and metabolism. More precisely, among others, phosphorylated AMPK stimulates glucose uptake by modulating GLUT-4 plasma membrane function [46-49]. As described in Figures 2A and 2B, the loss of AIF was associated to a significant and specific kinetic phosphorylation/activation of AMPK at Thr172 and the subsequent mRNA overexpression of Glut-4, not Glut-1. This suggested an enhancement of glucose uptake mediated by GLUT-4, which was further substantiated by the blockade of 2-NBDG assimilation by the specific GLUT-4 inhibitor indinavir (Figure 2C). The

measurement of lactate release, a marker of anaerobic glycolysis, indicated that  $AIF^{-/Y}$  compensated the mitochondrial OXPHOS dysfunction through the reinforcement of this glycolytic pathway (Figure 2D). Interestingly, the anaerobic glycolytic shift appeared to be sufficient not only to maintain ATP levels (Figure 1I) but also to preserve  $AIF^{-/Y}$  viability (absence of cell death), which surprisingly remained very close to those of control (D0) MEFs (Figure 2E). The central role of AMPK and GLUT-4 in the enhancement of the glucose metabolism and the preservation of ATP levels and cell viability in the AIF KO MEFs was corroborated by the pharmacological inhibition of AMPK or GLUT-4 by dorsomorphin and indinavir, respectively [50; 51]. As described in Supplemental Figure 3 and Figure 2E, AMPK inhibition precluded Glut-4 mRNA overexpression and both Glut-4 mRNA downregulation and inhibition of GLUT-4-mediated glucose uptake/metabolism induced cell death in the AIF KO MEFs. Altogether, these results corroborated that the  $AIF^{-/Y}$  MEFs counterbalance the mitochondrial OXPHOS dysfunction by reprogramming their metabolism towards anaerobic glycolysis through an AMPK/GLUT-4 adaptive mechanism.

We next investigated whether the lack of cell death in  $AIF^{-/Y}$  MEFs was linked to cell cycle alterations. As demonstrated by BrdU/PI co-staining, contrary to what was reported in embryonic stem (ES) cells [52], the loss of AIF provoked cell cycle and cell proliferation arrest in MEFs. More precisely, compared to control MEFs (D0), in which about 15-20 % of the cell population was in the proliferative S cell cycle phase, D12 and D16 AIF KO MEFs showed less than 5 % of the population in S phase (Figure 2F). Surprisingly, the arrest of cell proliferation recorded in  $AIF^{-/Y}$  MEFs appeared to be associated with the kinetic activation of a ROS/P53/P21-mediated senescence pathway [53; 54], as confirmed by specific  $C_{12}$ FDG senescent  $\beta$ -galactosidase staining (with more than 60 % of positive senescent labeling at D16) and mRNA overexpression of the superoxide-induced genetic markers *Tp53* and *Cdkn1 $\alpha$*  (Figures 2F, G, H, I, J). Note that *Cdkn1 $\alpha$*  expression is tightly controlled by *Tp53* and that *Cdkn1 $\alpha$*  codes for P21, a potent cyclin-dependent kinase inhibitor [55]. As expected, the kinetic *Tp53* and *Cdkn1 $\alpha$*  mRNA overexpression provoked the progressive up-regulation of the P21 protein (Figure 2J). P21 induction by means of cyclin-dependent kinase CDK2 and CDK4/6 inhibition leads to dephosphorylation/activation of retinoblastoma protein (pRB) (Figure 2K), a well-established cell cycle regulator that, in non-phosphorylated state, inhibits cell cycle progression [55-58]. Indeed, ROS-induced senescence can be identified *in vitro* by the increased expression of genes/proteins associated with cell cycle arrest (such as P53 and P21), the pRB dephosphorylation/activation, and the presence of senescence-associated  $\beta$ -galactosidase activity, which is attributed to the high lysosomal content of senescent cells [59]. All these features characterized  $AIF^{-/Y}$  MEFs.

### **3.2 $AIF^{-/Y}$ MEFs were resistant to caspase-independent cell death.**



After remaining senescent for days, about 2% of  $AIF^{+/Y}$  MEFs spontaneously proliferated. The analysis of these proliferating cells indicated that, compared to the senescent  $AIF^{+/Y}$  MEFs, cycling AIF KO MEFs diminished the mitochondrial mass and the ROS levels. This was correlated to the loss of P21 expression and the subsequent phosphorylation/inactivation of pRb that favors cell cycle progression (Supplemental Fig. 4). These results support the relationship between ROS generation and P21/pRb-mediated cell cycle arrest in the senescent AIF KO cells.

We used proliferating AIF KO MEFs to analyze, among others, the programmed cell death capacities of  $AIF^{+/Y}$  cells. To generate a reliable control, we reintroduced the AIF-wt cDNA (V5 tagged) into the  $AIF^{+/Y}$  MEFs by lentiviral transduction (AIF KO + AIF-V5 MEFs). AIF KO + AIF-V5 MEFs incorporated AIF into the mitochondria, rescued the normal mitochondrial network (Figure 3A), and reconstituted the ETC proteins (Figure 3B) and the SC patterns (Figure 3C). The functionality of mitochondrial OXPHOS in the AIF KO + AIF-V5 MEFs was substantiated by oxygen consumption tests (Figure 3D). Finally, we observed that the glycolytic adaptive phenotype of  $AIF^{+/Y}$  MEFs was disabled by the lentiviral AIF transduction (Figure 3E and F). Concerning sensitivity to PCD, contrary to primary (WT) and the reconstituted AIF KO + AIF-V5 MEFs,  $AIF^{+/Y}$  MEFs were sensitive to the glycolytic inhibitor 2-Deoxyglucose (Figure 3G), underlining its glucose dependency. Additionally, cell lines were exposed to different PCD inducers: MNNG and  $\beta$ -Lapachone (caspase-independent PCD inducers) [10; 18; 20; 21; 60], STS (a cytotoxic inducer partially controlled by caspase activation) and etoposide (a typical caspase-dependent agent) [61-63]. As depicted in Figure 3H,  $AIF^{+/Y}$  MEFs were highly resistant to MNNG and  $\beta$ -Lapachone, partially resistant to STS, and sensitive to etoposide. We corroborated that the pretreatment of MEFs with the broad caspase inhibitor (QVD.OPh) inhibited etoposide-mediated killing. Finally, as expected, reintroduction of AIF into the  $AIF^{+/Y}$  MEFs fully re-sensitized MEFs to MNNG,  $\beta$ -Lapachone, and STS. Altogether, these results substantiate the relevance of AIF in caspase-independent cell death and corroborate the previously described limited response of AIF-deficient MEFs to STS [14; 21]. Finally, those data indicate that  $AIF^{+/Y}$  MEFs remain sensitive to caspase-dependent PCD inducers.

### **3.3 A significant percentage of $AIF^{+/-}$ females developed a hydrocephalus phenotype and exhibited immune cell exhaustion.**

To extend our study towards an *in vivo* model, we crossed *Aifm1* floxed males ( $AIF^{Fl/Y}$ ) with a PGK-Cre strain, which drives Cre recombinase expression very early during embryonic development [64]. This crossbreeding yielded heterozygous female offspring ( $AIF^{+/-}$ ) in a Mendelian distribution (Figure 4A). Most of the  $AIF^{+/-}$  animals did not present external phenotypic changes until they reached 6 months of age, at which stage we detected a significant diminution of

bone marrow, spleen and thymus cellularity (Supplemental Fig. 5). Surprisingly, about 10% of  $AIF^{+/-}$  females (5% of total newborns) developed a perinatal hydrocephalus phenotype (visible in two-week old animals) characterized by an enlarged and dome-shaped head accompanied by a progressive loss of mobility (Figure 4A). These animals died around 5 weeks after birth. Compared to control animals, the brain of  $AIF^{+/-}$  hydrocephalus animals ( $AIF^{+/-}$  HC) showed an excess of cerebrospinal fluid (CSF) that warped the brain (right microphotographs in Figure 4A). Hematoxylin/eosin staining of mice and head sections shed light on the extent to which the CSF compressed the cerebral mass into the cranial cavity (Figure 4B, left microphotographs). In coronal sections, we observed severe thinning of brain ventricular wall with an enlargement of the lateral ventricles and meningeal fibrosis (Figure 4B, right panels). Brain development, apart from the compression, seemed normal. Some mice showed a dilated third ventricle and a herniated cerebellum. We also noticed strong spinal and parenchymatous haemorrhages. Circulating macrophages engorged with blood could be observed in some sections of the ependymal epithelium (Figure 4C). This epithelium, lining the ventricular cavities, is normally composed of a single cell layer. In the case of  $AIF^{+/-}$  HC, the ependymal epithelium lining the ventricles was abnormal with visible defects of ciliation. Additionally,  $AIF^{+/-}$  HC mice presented immature "neuroblast" foci with abnormal structures (Figure 4C). These structures, which normally disappear at the closure of the neural tube, indicated some defects in the development of the  $AIF^{+/-}$  HC. The hydrocephalus mice also had a bone structure problem, probably due to the cranial cavity swelling provoked by the CSF pressure. No apoptotic features were observed on the histological sections.  $AIF^{+/-}$  HC mice did not exhibit apparent neurodegeneration and had a normal neuronal organization. Interestingly, a protein carbonylation immunoblot approach performed on brain homogenates from 2.5 week-old animals revealed that, compared to  $AIF^{+/+}$  and non-HC  $AIF^{+/-}$  females, the brain of the  $AIF^{+/-}$  HC females displayed higher ROS levels (Figure 4D). This suggested a relationship between ROS excess, generated by OXPHOS dysfunction, and perinatal hydrocephaly. This hypothesis was corroborated by the addition of an antioxidant (riboflavin) in the drinking water of the dams, which significantly reduced the occurrence of the  $AIF^{+/-}$  HC phenotype and microglial activation, detected by Iba1 immunolabeling, reflecting the inflammatory process provoked by brain squeezing (Figures 4E and F). The mobility of riboflavin-treated  $AIF^{+/-}$  females also appeared normal, indicating that the addition of an antioxidant in the drinking water of  $AIF^{+/-}$  mice rescues the WT phenotype.

### **3.4 AIF loss in mouse embryo induced midgestation lethality associated with energy loss, proliferation arrest and increased apoptosis.**

Next, we tried to generate AIF KO mice by crossing the non-HC  $AIF^{+/-}$  females with WT males. Unfortunately, this crossing only generated  $AIF^{+/+}$  and  $AIF^{+Y}$  animals, suggesting embryonic

lethality of the  $AIF^{-/Y}$  and  $AIF^{+/-}$  progeny (Figure 5A, birth animals). Indeed,  $AIF^{-/Y}$  male embryos presented a normal development only until E7.5 (Figure 5A and B). Then, they displayed growth delay and arrested development between E8.5 and E9.5, leading to embryo death at E11.5 (Figure 5A, B, and C). Female  $AIF^{+/-}$  embryos exhibited inconstant developmental phenotypes and died around E13.5 (Figure 5A).

We scrutinized mitochondrial and metabolic alterations associated to lethality of  $AIF^{-/Y}$  embryos. An electronic microscopy approach revealed highly fragmented mitochondria in E9.5  $AIF^{-/Y}$  embryos (Figure 5D). Immunoblot analysis of key mitochondrial ETC proteins showed dramatic reduction of NDUFA9 (complex I protein) and COX4I2 (complex IV protein) (Figure 5E). This was accompanied by an impairment of mitochondrial OXPHOS, as demonstrated by a COX/SDH histochemical labeling (Figure 5F): indeed, sections from mutant E9.5 embryos failed to show the dark staining characterizing OXPHOS functionality. As a consequence of OXPHOS dysfunction,  $AIF^{-/Y}$  embryos exhibited very low ATP levels (Figure 5G). Surprisingly, as shown by the low amount of lactate detected (Figure 5H),  $AIF^{-/Y}$  embryos appeared unable to reprogram their metabolism towards anaerobic glycolysis, contrary to  $AIF^{-/Y}$  MEFs (Figure 2). Moreover, histological analysis showed that these mitochondrial/metabolic changes were accompanied by a decrease in the proliferation rate starting at E.8.5 (Figure 6A) and by the enhancement of apoptosis at E.9.5 in  $AIF^{-/Y}$  embryos (Figure 6B).

Finally, taking into consideration the inability of the  $AIF^{-/Y}$  embryos to reprogram their metabolism towards anaerobic glycolysis, we tried to circumvent lethality by eliminating the excess of ROS with riboflavin and feeding the dams with a high fat diet (HFD) in which the major source of energy changed from carbohydrates to fatty acids, which have proved to be efficient in other AIF deficient models [65]. However, even in these alternative conditions, we were unable to generate  $AIF^{-/Y}$  and  $AIF^{+/-}$  animals (Supplemental Fig. 6). Overall, these data corroborated the mitochondrial OXPHOS/metabolism dysfunction of  $AIF^{-/Y}$  embryos, and their incapacity to reprogram their metabolism in order to grow and differentiate.

By creating an *AIF* KO model that enables *in vitro* and *in vivo* analysis, we bring to light new cellular and developmental consequences of the loss of mitochondrial AIF. We show that AIF deficiency triggers a destabilization of the mitochondrial ETC complexes I and IV, leading to supercomplex disorganization, mitochondrial transmembrane potential loss, and high levels of ROS generation. *AIF*<sup>-Y</sup> MEFs counterbalance these OXPHOS alterations by a mitochondrial network reorganization implicating a fusion process and the overexpression of the mitochondrial SOD2. A more accurate molecular analysis at cellular, embryonic, and adult mice levels indicates that the mitochondrial OXPHOS dysfunction associated to AIF loss results in pleiotropic effects: (i) at a cellular level, *AIF*<sup>-Y</sup> MEFs boost their anaerobic glycolytic metabolism and evolve towards a senescence phenotype. The glycolytic phenotype is characterized by AMPK phosphorylation/activation, the overexpression of the glucose assimilation transporter GLUT-4, the enhancement of glucose uptake, and anaerobic lactate generation. The energy-sensing kinase AMPK and the glucose assimilation transporter GLUT-4 play central roles in the glycolytic reprogramming of the AIF KO MEFs. Based on these results, it will be interesting to analyze in future studies the transcriptional drivers activated by AMPK to specifically modulate *Glut-4* expression and to control the metabolic adaptive responses that run the *AIF*<sup>-Y</sup> MEFs towards senescence. Concerning the senescent phenotype, the ROS excess associated to OXPHOS dysfunction provokes overexpression of *Tp53* and *Cdkn1α*, two genes associated with cell cycle arrest, as well as up-regulation of P21, a protein that, by provoking the activation/dephosphorylation of pRB, inhibits cell cycle progression. Strikingly, a small percentage of *AIF*<sup>-Y</sup> MEFs spontaneously proliferate. These cycling AIF KO MEFs diminish the mitochondrial mass and regulate ROS levels, thus inactivating the senescent pathway. Remarkably, the cycling *AIF*<sup>-Y</sup> MEFs are resistant to caspase-independent inducers, underlining the role of AIF in this mode of PCD and avoiding previous controversies on the participation of AIF in cell death; (ii) in whole animal experiments, we have confirmed that the AIF KO animals are embryonic lethal. However, analysis of heterozygous *AIF*<sup>+/-</sup> females has originally uncovered immune cell exhaustion and the development of perinatal hydrocephalus seemingly associated to an excess of mitochondrial ROS. This phenotype is characterized by an excess of cerebrospinal fluid, brain development impairment, meningeal fibrosis, and medullar hemorrhages; (iii) finally, our findings lead us to propose that AIF-deficient embryonic lethality is linked to the inability of KO embryos to reprogram their metabolism towards anaerobic glycolysis. This provokes dramatic ATP loss, arrest in proliferation, and caspase-dependent embryo death.

The mitochondrial “pro-survival” function of AIF seems linked to its role in the import and assembly of key proteins of the ETC complexes [12; 66]. Our results in MEFs and embryos, analyzed within the context of the “plasticity” model of ETC supercomplex organization [8; 41], indicate that AIF loss provokes disorganization of the SC architecture, OXPHOS deregulation, ROS overproduction, and a very restricted capacity for mitochondrial ATP generation. However, AIF deficiency does not fully yield defective mitochondria in MEFs, as demonstrated by the assessment of individual mitochondrial complex activities, which reveal a limited but still functional ETC (amytal inhibits the residual complex I activity). Indeed, our data on the overgeneration of mitochondrial ROS in the absence of mitochondrial ATP generation strongly suggest that the ETC of the AIF<sup>-Y</sup> MEFs is somewhat functional, but the loss of key complex I/IV proteins provokes an impairment. As a consequence, the AIF KO mitochondria appear unable to generate the electrochemical gradient needed to produce ATP, probably by a premature electron leakage (which generates the excess of ROS detected). Very surprisingly, this mitochondrial ETC dysfunction does not lead to cell death. Instead, AIF<sup>-Y</sup> MEFs reprogram their metabolism toward AMPK/GLUT-4-mediated anaerobic glycolysis (to generate ATP), overexpress ROS detoxifying enzymes (to regulate the excess of ROS as much as possible), and activate an enzymatically controlled senescent pathway. It seems, therefore, that MEFs have the plasticity to respond to ETC weakening. In contrast, AIF<sup>-Y</sup> embryos are unable to perform this metabolic adaptive response and show a drastic developmental defect leading to death. What is the reason for the different MEFs/embryo behavior? We could hypothesize that the *in vitro* carbohydrate-enriched cell culture condition supports MEFs glycolytic metabolic reprogramming. *In vivo*, a glycolytic versus OXPHOS metabolic shift around E8.5 has been described to be essential for embryonic survival and fetal development [67; 68]. In AIF<sup>-Y</sup> OXPHOS dysfunctional embryos, this shift is probably impossible, yielding an inevitable embryonic death.

Apart from its mitochondrial OXPHOS function, AIF has a lethal role upon its translocation to the nucleus [18-21; 69]. Strong evidence for an AIF role in PCD has come from studies performed in a large number of cell death models [21; 22; 70-76]. Despite this substantial amount of work, some controversy remains about AIF function in PCD. Indeed, certain studies performed in HeLa cells, SV40-immortalized MEFs, or with caspase-dependent apoptotic inducers, have raised doubts about the apoptogenic AIF potential [14; 77; 78]. We tried to elucidate this issue by verifying the response to typical caspase-dependent and independent inducers in non-transformed WT, AIF<sup>-Y</sup>, and AIF KO + AIF reconstituted cells. We found that AIF<sup>-Y</sup> MEFs are significantly resistant to treatment with MNNG and  $\beta$ -Lapachone, classical caspase-independent PCD inducers, but they remain sensitive to caspase-dependent apoptotic drugs. Although a more exhaustive work is required, our results already indicate that the contradictory results on the role AIF plays in PCD

could be merely associated to the cellular system employed or the PCD inducer tested. In any case, the phenotype of  $AIF^{F/Y}$  MEFs confirms the relevance of AIF in the control of caspase-independent PCD.

Genetic inactivation of AIF provokes embryonic death. Consequently, it is not possible to generate an AIF KO progeny. Previous studies in embryoid bodies have suggested that AIF could regulate the initial stages of murine development by controlling the cell death process of cavitation [79]. However, in the present work, we show that  $AIF^{F/Y}$  embryos develop normally until E7.5 and are morphologically indistinguishable from WT embryos. By E8.5,  $AIF^{F/Y}$  embryos are delayed compared to WT littermates. Between E8.5 and E9.5 they stop growing, fail to turn, and have abnormal brain development.  $AIF^{F/Y}$  embryos finally die at around E11.5. These results are consistent with another study indicating that AIF and the mitochondrial OXPHOS are not required at the initial stages of mouse development [52]. However, in contrast to this work, we have observed arrest of proliferation and enhancement of PCD in E8.5 and E9.5  $AIF^{F/Y}$  embryos. In addition, we have found that OXPHOS dysfunction associated to AIF loss and the incapacity to perform metabolic reprogramming seemed key to the embryonic lethality associated with AIF deficiency.

In future research, it will be interesting to understand why it is possible to generate  $AIF^{+/-}$  offspring from  $AIF^{F/Y}$ ; PGK-Cre cross while, in contrast, the resulting  $AIF^{+/-}$  females are unable to generate heterozygous AIF progeny. An exciting possibility is the existence of a bias in the timing or strength of allele expression depending on the paternal or maternal origin of the X-chromosome. In fact, our data suggest that the E8.5 “embryonic-shift” from anaerobic to aerobic metabolism can only occur when the female transmits the wild-type allele. This has no incidence in the  $AIF^{F/Y}$  and PGK-Cre crossing (having an AIF KO allele generated by PGK-Cre in the floxed X-chromosome coming from the male). In the case of the progeny of  $AIF^{+/-}$  females, the AIF KO allele transmitted by the dams would be unable to perform the “embryonic-shift”, resulting in the death of the  $AIF^{+/-}$  and  $AIF^{F/Y}$  embryos. A second possibility, with similar embryonic death consequences, is the implication of *Aifm1* in the particular behavior of the paternal X chromosome (Xp). Indeed, it has been well documented that the Xp chromosome is preferentially inactivated during the first stages of mice development [80; 81]. Similarly, there is evidence that some genes are initially expressed from the maternal allelic form [82]. In our case, the *Aifm1*-mutated maternal allelic form would not be able to generate AIF. If *Aifm1* was also inactivated in Xp, the mitochondria of the  $AIF^{+/-}$  and  $AIF^{F/Y}$  embryos would be dysfunctional and, consequently, the embryo would not be viable. In favor of this second possibility is the morphological analysis of the mitochondria from AIF-mutated embryo (Figure 5D and Supplemental Fig. 7), which reveals the irregular structure associated to mitochondrial dysfunction [35].

The  $AIF^{-/+}$  females show two relevant pathological phenotypes: (i) an immune exhaustion in the adult animals and (ii) a perinatal hydrocephalus phenotype. Concerning the alterations in the immune system associated to AIF, an initial study had been done in the Hq strain. Here, low AIF expression led to high susceptibility of T-cell blasts to activation-induced cell death and reduced sensitivity to neglect-induced cell death. Moreover, thymocytes from Hq mice exhibited higher ROS levels, which impacted thymocyte and T-cell development [31; 83]. A more specific work in which *Aif* was ablated around the DN3 stage of thymocyte development reported that AIF-loss had no impact on T-cell development. The use of the CD19-cre mice strain indicated that AIF was not required for B-cell development and function [14]. Our recent work, performed in a *bona fide* hematopoietic AIF KO strain, where the protein was ablated very early during hematopoiesis, revealed a greater role for AIF in immune cell fate [35; 36]. Indeed, the loss of AIF provoked a progressive exhaustion of the HSC pool and developmental defaults in the thymocyte, T-cell, B-cell, and erythroid lineages. In agreement with these results, we observed a progressive cellular exhaustion in the bone marrow, spleen and thymus of the  $AIF^{-/+}$  females, thus fully corroborating the relevance of AIF in the fine-tuning of the immune system.

Previously unreported is the hydrocephalus phenotype observed in about 10% of  $AIF^{+/-}$  newborns. The signs of the  $AIF^{-/+}$  hydrocephaly are readily apparent in young animals that develop the disease before the cranial sutures close (allowing for an enlarged and domed head). This is accompanied by a progressive loss of animal mobility, certainly caused by the fact that the brain is completely encased within the bony calvarium. The build-up of CSF causes tissue inflammation (depicted by the microglial activation), haemorrhages of the surrounding brain tissue, enlargement of the ventricles, and herniation of the brain and cerebellum. In a general perspective, hydrocephalus may be caused by a blockage of the normal flow of CSF, a failure of absorption of CSF or, less commonly, an overproduction of CSF. CSF circulates throughout the ventricular brain system through the motion of the ciliated ependymal cells that line the ventricles. In  $AIF^{-/+}$  HC, we detected that the ependymal epithelium was absent from the edge of the ventricles and, consequently, presented loss of ciliation. Thus, similarly to what has been described in other mice strains [84-88], we propose that  $AIF^{-/+}$  hydrocephalus is caused by defects of the normal CSF flow associated to the loss of ciliated ependymal cells. This cellular loss appears to be directly related to the excess of ROS detected in the brain homogenates of the  $AIF^{-/+}$  HC animals. Indeed, an external control of ROS excess through the supply of riboflavin to the dams and newborns is enough to reduce this phenotype to the standards of the C57BL/6J strain [89]. Interestingly, riboflavin was given to patients with mitochondrial myopathy due to OXPHOS deficiency [90-92]. In fact, riboflavin is a precursor to FMN and FAD, which are cofactors of ETC complexes I and II, respectively. Riboflavin has been proposed to act therapeutically through several potential

mechanisms including ROS control and inhibition of the breakdown of complex I by providing more resistance to proteolysis or stabilizing the mitochondrial membrane [92].

## 5. CONCLUSION

Our data reveal that the mitochondrial signals regulated by AIF are critical to cellular decision-making. Emerging as a link between mitochondrial metabolism, mouse development, and cell fate, AIF-mediated OXPHOS regulation represents a potential target in the development of new therapeutic approaches. Indeed, a better knowledge of how the cells can modify their metabolic pathways may enable us to manipulate them. Ultimately, this might lead to new treatment options for diseases in which the mitochondrial OXPHOS alteration/dysfunction has an instrumental role.

Journal Pre-proof



We thank the animal facility staff (CEF Cordeliers, Paris, France) for mice housing support, Kevin Garbin and Danielle Chateau for help in electron microscopy, Pascal Ezan for help in protein extraction, Patricia Flamant and Patrick Avé for help in brain and embryo immunohistochemistry (Human histopathology and animal models unit, Pasteur Institute), Marie-Annick Thomas for advice on brain assessments, and M. Segade for proofreading. This work was supported by Fondation ARC (PJA20151203407 and PJA20171206551), Fondation pour la Recherche Médicale, French National Research Agency (ANR-09-BLAN-0247), and the SIRIC-CURAMUS (INCA-DGOS-Inserm\_12560). L.C. received PhD fellowship support from ENS-Cachan, Société Française d'Hématologie, and Fondation ARC. N.M. received a fellowship of the FRS/FRIA. I.M. is a FNRS research associate and an investigator of WELBIO.

### **AUTHOR CONTRIBUTIONS**

L.D. designed experiments, performed *in vitro* and *in vivo* studies, interpreted the data and helped to write the manuscript. N.M., L.C., M.-N.B.-N., L.K.L., M.T., A.M., A.P., R.M.-L., M.B., L.V., D.G. designed experiments, performed *in vitro* and/or *in vivo* work and analyzed the results. K.G. carried out electron microscopy. C.L. provided key reagents, organized Clark electrode oxygen consumption assays and analyzed the results. F.L. provided the PGK-Cre strain and helped in the development of the *Aifm1* floxed mice. M.C-S. participated in the development of the *Aifm1* floxed mice and helped to write the manuscript. P.F.-S. set-up the mitochondrial supercomplex analyses and interpreted the data. F.C. provided reagents, designed the assessment of the hydrocephalus animals and analyzed the results. I.M. provided reagents, performed experiments, designed the embryonic tests, interpreted the data and helped to write the manuscript. S.A.S. designed *in vitro* and *in vivo* studies, coordinated and supervised the study, interpreted the data and wrote the manuscript.

### **CONFLICT OF INTEREST**

The authors declare no conflict of interest.

- [1] MacIver, N.J., Michalek, R.D., Rathmell, J.C., 2013. Metabolic regulation of T lymphocytes. *Annu Rev Immunol* 31:259-283.
- [2] Pearce, E.L., Poffenberger, M.C., Chang, C.H., Jones, R.G., 2013. Fueling immunity: insights into metabolism and lymphocyte function. *Science* 342(6155):1242-454.
- [3] Holmstrom, K.M., Finkel, T., 2014. Cellular mechanisms and physiological consequences of redox-dependent signalling. *Nat Rev Mol Cell Biol* 15(6):411-421.
- [4] Pearce, E.L., Pearce, E.J., 2013. Metabolic pathways in immune cell activation and quiescence. *Immunity* 38(4):633-643.
- [5] Folmes, C.D., Dzeja, P.P., Nelson, T.J., Terzic, A., 2012. Metabolic plasticity in stem cell homeostasis and differentiation. *Cell Stem Cell* 11(5):596-606.
- [6] Sena, L.A., Chandel, N.S., 2012. Physiological roles of mitochondrial reactive oxygen species. *Mol Cell* 48(2):158-167.
- [7] Hamanaka, R.B., Chandel, N.S., 2010. Mitochondrial reactive oxygen species regulate cellular signaling and dictate biological outcomes. *Trends Biochem Sci* 35(9):505-513.
- [8] Lapuente-Brun, E., Moreno-Loshuertos, R., Acin-Perez, R., Latorre-Pellicer, A., Colas, C., Balsa, E., et al., 2013. Supercomplex assembly determines electron flux in the mitochondrial electron transport chain. *Science* 340(6140):1567-1570.
- [9] Acin-Perez, R., Enriquez, J.A., 2014. The function of the respiratory supercomplexes: the plasticity model. *Biochim Biophys Acta* 1837(4):444-450.
- [10] Klein, J.A., Longo-Guess, C.M., Rossmann, M.P., Seburn, K.L., Hurd, R.E., Frankel, W.N., et al., 2002. The harlequin mouse mutation downregulates apoptosis-inducing factor. *Nature* 419(6905):367-374.
- [11] Pospisilik, J.A., Knauf, C., Joza, N., Benit, P., Orthofer, M., Cani, P.D., et al., 2007. Targeted deletion of AIF decreases mitochondrial oxidative phosphorylation and protects from obesity and diabetes. *Cell* 131(3):476-491.
- [12] Hangen, E., Feraud, O., Lachkar, S., Mou, H., Doti, N., Fimia, G.M., et al., 2015. Interaction between AIF and CHCHD4 Regulates Respiratory Chain Biogenesis. *Mol Cell* 58(6):1001-1014.
- [13] Meyer, K., Buettner, S., Ghezzi, D., Zeviani, M., Bano, D., Nicotera, P., 2015. Loss of apoptosis-inducing factor critically affects MIA40 function. *Cell Death Dis* 6:e1814.
- [14] Milasta, S., Dillon, C.P., Sturm, O.E., Verbist, K.C., Brewer, T.L., Quarato, G., et al., 2016. Apoptosis-Inducing-Factor-Dependent Mitochondrial Function Is Required for T Cell but Not B Cell Function. *Immunity* 44(1):88-102.
- [15] Ishimura, R., Martin, G.R., Ackerman, S.L., 2008. Loss of apoptosis-inducing factor results in cell-type-specific neurogenesis defects. *J Neurosci* 28(19):4938-4948.
- [16] Benit, P., Goncalves, S., Dassa, E.P., Briere, J.J., Rustin, P., 2008. The variability of the harlequin mouse phenotype resembles that of human mitochondrial-complex I-deficiency syndromes. *PLoS One* 3(9):e3208.
- [17] Cheung, E.C., Joza, N., Steenaert, N.A., McClellan, K.A., Neuspiel, M., McNamara, S., et al., 2006. Dissociating the dual roles of apoptosis-inducing factor in maintaining mitochondrial structure and apoptosis. *EMBO J* 25(17):4061-4073.
- [18] Artus, C., Boujrad, H., Bouharrou, A., Brunelle, M.N., Hoos, S., Yuste, V.J., et al., 2010. AIF promotes chromatinolysis and caspase-independent programmed necrosis by interacting with histone H2AX. *EMBO J* 29(9):1585-1599.

- [19] Baritaud, M., Cabon, L., Delavallee, L., Galan-Malo, P., Gilles, M.E., Brunelle-Navas, M.N., et al., 2012. AIF-mediated caspase-independent necroptosis requires ATM and DNA-PK-induced histone H2AX Ser139 phosphorylation. *Cell Death Dis* 3:e390.
- [20] Cabon, L., Galan-Malo, P., Bouharrou, A., Delavallee, L., Brunelle-Navas, M.N., Lorenzo, H.K., et al., 2012. BID regulates AIF-mediated caspase-independent necroptosis by promoting BAX activation. *Cell Death Differ* 19(2):245-256.
- [21] Moubarak, R.S., Yuste, V.J., Artus, C., Bouharrou, A., Greer, P.A., Menissier-de Murcia, J., et al., 2007. Sequential Activation of Poly(ADP-Ribose) Polymerase 1, Calpains, and Bax Is Essential in Apoptosis-Inducing Factor-Mediated Programmed Necrosis. *Mol Cell Biol* 27(13):4844-4862.
- [22] Yu, S.W., Wang, H., Poitras, M.F., Coombs, C., Bowers, W.J., Federoff, H.J., et al., 2002. Mediation of poly(ADP-ribose) polymerase-1-dependent cell death by apoptosis-inducing factor. *Science* 297(5579):259-263.
- [23] Xu, Y., Huang, S., Liu, Z.G., Han, J., 2006. Poly(ADP-ribose) Polymerase-1 Signaling to Mitochondria in Necrotic Cell Death Requires RIP1/TRAF2-mediated JNK1 Activation. *J Biol Chem* 281(13):8788-8795.
- [24] Benit, P., Pelhaitre, A., Saunier, E., Bortoli, S., Coulibaly, A., Rak, M., et al., 2017. Paradoxical Inhibition of Glycolysis by Pioglitazone Opposes the Mitochondriopathy Caused by AIF Deficiency. *EBioMedicine* 17:75-87.
- [25] Ghezzi, D., Sevrioukova, I., Invernizzi, F., Lamperti, C., Mora, M., D'Adamo, P., et al., 2010. Severe X-linked mitochondrial encephalomyopathy associated with a mutation in apoptosis-inducing factor. *Am J Hum Genet* 86(4):639-649.
- [26] Berger, I., Ben-Neriah, Z., Dor-Wolman, T., Shaag, A., Saada, A., Zenvirt, S., et al., 2011. Early prenatal ventriculomegaly due to an AIFM1 mutation identified by linkage analysis and whole exome sequencing. *Mol Genet Metab* 104(4):517-520.
- [27] Diodato, D., Tasca, G., Verrigni, D., D'Amico, A., Rizza, T., Tozzi, G., et al., 2016. A novel AIFM1 mutation expands the phenotype to an infantile motor neuron disease. *Eur J Hum Genet* 24(3):463-466.
- [28] Sancho, P., Sanchez-Montegudo, A., Collado, A., Marco-Marin, C., Dominguez-Gonzalez, C., Camacho, A., et al., 2017. A newly distal hereditary motor neuropathy caused by a rare AIFM1 mutation. *Neurogenetics* 18(4):245-250.
- [29] Shen, S.M., Guo, M., Xiong, Z., Yu, Y., Zhao, X.Y., Zhang, F.F., et al., 2015. AIF inhibits tumor metastasis by protecting PTEN from oxidation. *EMBO Rep* 16(11):1563-1580.
- [30] Li, T., Li, K., Zhang, S., Wang, Y., Xu, Y., Cronin, S.J.F., et al., 2020. Overexpression of apoptosis inducing factor aggravates hypoxic-ischemic brain injury in neonatal mice. *Cell Death Dis* 11(1):77.
- [31] Srivastava, S., Banerjee, H., Chaudhry, A., Khare, A., Sarin, A., George, A., et al., 2007. Apoptosis-inducing factor regulates death in peripheral T cells. *J Immunol* 179(2):797-803.
- [32] van Empel, V.P., Bertrand, A.T., van Oort, R.J., van der Nagel, R., Engelen, M., van Rijen, H.V., et al., 2006. EUK-8, a superoxide dismutase and catalase mimetic, reduces cardiac oxidative stress and ameliorates pressure overload-induced heart failure in the harlequin mouse mutant. *J Am Coll Cardiol* 48(4):824-832.
- [33] Chung, S.H., Calafiore, M., Plane, J.M., Pleasure, D.E., Deng, W., 2011. Apoptosis inducing factor deficiency causes reduced mitofusion 1 expression and patterned Purkinje cell degeneration. *Neurobiol Dis* 41(2):445-457.

- [34] Joza, N., Oudit, G.Y., Brown, D., Benit, P., Kassiri, Z., Vahsen, N., et al., 2005. Muscle-specific loss of apoptosis-inducing factor leads to mitochondrial dysfunction, skeletal muscle atrophy, and dilated cardiomyopathy. *Mol Cell Biol* 25(23):10261-10272.
- [35] Cabon, L., Bertaux, A., Brunelle-Navas, M.N., Nemazanyy, I., Scourzic, L., Delavallee, L., et al., 2018. AIF loss deregulates hematopoiesis and reveals different adaptive metabolic responses in bone marrow cells and thymocytes. *Cell Death Differ* 25(5):983-1001.
- [36] Bertaux, A., Cabon, L., Brunelle-Navas, M.N., Bouchet, S., Nemazanyy, I., Susin, S.A., 2018. Mitochondrial OXPHOS influences immune cell fate: lessons from hematopoietic AIF-deficient and NDUFS4-deficient mouse models. *Cell Death Dis* 9(6):581.
- [37] Hameyer, D., Loonstra, A., Eshkind, L., Schmitt, S., Antunes, C., Groen, A., et al., 2007. Toxicity of ligand-dependent Cre recombinases and generation of a conditional Cre deleter mouse allowing mosaic recombination in peripheral tissues. *Physiol Genomics* 31(1):32-41.
- [38] Zhang, J., Nuebel, E., Wisidagama, D.R., Setoguchi, K., Hong, J.S., Van Horn, C.M., et al., 2012. Measuring energy metabolism in cultured cells, including human pluripotent stem cells and differentiated cells. *Nat Protoc* 7(6):1068-1085.
- [39] Stewart, S.A., Dykxhoorn, D.M., Palliser, D., Mizuno, H., Yu, E.Y., An, D.S., et al., 2003. Lentivirus-delivered stable gene silencing by RNAi in primary cells. *RNA* 9(4):493-501.
- [40] Ross, J.M., Oberg, J., Brene, S., Coppotelli, G., Terzioglu, M., Pernold, K., et al., 2010. High brain lactate is a hallmark of aging and caused by a shift in the lactate dehydrogenase A/B ratio. *Proc Natl Acad Sci U S A* 107(46):20087-20092.
- [41] Dudkina, N.V., Kouril, R., Peters, K., Braun, H.P., Boekema, E.J., 2010. Structure and function of mitochondrial supercomplexes. *Biochim Biophys Acta* 1797(6-7):664-670.
- [42] Herzig, S., Shaw, R.J., 2018. AMPK: guardian of metabolism and mitochondrial homeostasis. *Nat Rev Mol Cell Biol* 19(2):121-135.
- [43] Rabinovitch, R.C., Samborska, B., Faubert, B., Ma, E.H., Gravel, S.P., Andrzejewski, S., et al., 2017. AMPK Maintains Cellular Metabolic Homeostasis through Regulation of Mitochondrial Reactive Oxygen Species. *Cell Rep* 21(1):1-9.
- [44] Gwinn, D.M., Shackelford, D.B., Egan, D.F., Mihaylova, M.M., Mery, A., Vasquez, D.S., et al., 2008. AMPK phosphorylation of raptor mediates a metabolic checkpoint. *Mol Cell* 30(2):214-226.
- [45] Sanli, T., Steinberg, G.R., Singh, G., Tsakiridis, T., 2014. AMP-activated protein kinase (AMPK) beyond metabolism: a novel genomic stress sensor participating in the DNA damage response pathway. *Cancer Biol Ther* 15(2):156-169.
- [46] Hardie, D.G., Ross, F.A., Hawley, S.A., 2012. AMPK: a nutrient and energy sensor that maintains energy homeostasis. *Nat Rev Mol Cell Biol* 13(4):251-262.
- [47] Holmes, B.F., Kurth-Kraczek, E.J., Winder, W.W., 1999. Chronic activation of 5'-AMP-activated protein kinase increases GLUT-4, hexokinase, and glycogen in muscle. *J Appl Physiol* (1985) 87(5):1990-1995.
- [48] McGee, S.L., van Denderen, B.J., Howlett, K.F., Mollica, J., Schertzer, J.D., Kemp, B.E., et al., 2008. AMP-activated protein kinase regulates GLUT4 transcription by phosphorylating histone deacetylase 5. *Diabetes* 57(4):860-867.
- [49] Ojuka, E.O., Jones, T.E., Nolte, L.A., Chen, M., Wamhoff, B.R., Sturek, M., et al., 2002. Regulation of GLUT4 biogenesis in muscle: evidence for involvement of AMPK and Ca<sup>2+</sup>. *Am J Physiol Endocrinol Metab* 282(5):E1008-1013.

- [50] Bahne, E., Sun, E.W.L., Young, R.L., Hansen, M., Sonne, D.P., Hansen, J.S., et al., 2018. Metformin-induced glucagon-like peptide-1 secretion contributes to the actions of metformin in type 2 diabetes. *JCI Insight* 3(23).
- [51] Hresko, R.C., Hruz, P.W., 2011. HIV protease inhibitors act as competitive inhibitors of the cytoplasmic glucose binding site of GLUTs with differing affinities for GLUT1 and GLUT4. *PLoS One* 6(9):e25237.
- [52] Brown, D., Yu, B.D., Joza, N., Benit, P., Meneses, J., Firpo, M., et al., 2006. Loss of Aif function causes cell death in the mouse embryo, but the temporal progression of patterning is normal. *Proc Natl Acad Sci U S A* 103(26):9918-9923.
- [53] Munoz-Espin, D., Serrano, M., 2014. Cellular senescence: from physiology to pathology. *Nat Rev Mol Cell Biol* 15(7):482-496.
- [54] Martinez-Zamudio, R.I., Robinson, L., Roux, P.F., Bischof, O., 2017. SnapShot: Cellular Senescence Pathways. *Cell* 170(4):816-816 e811.
- [55] Broude, E.V., Swift, M.E., Vivo, C., Chang, B.D., Davis, B.M., Kalurupalle, S., et al., 2007. p21(Waf1/Cip1/Sdi1) mediates retinoblastoma protein degradation. *Oncogene* 26(48):6954-6958.
- [56] Sherr, C.J., McCormick, F., 2002. The RB and p53 pathways in cancer. *Cancer Cell* 2(2):103-112.
- [57] Zheng, L., Lee, W.H., 2001. The retinoblastoma gene: a prototypic and multifunctional tumor suppressor. *Exp Cell Res* 264(1):2-18.
- [58] Leinicke, J.A., Longshore, S., Wakeman, D., Guo, J., Warner, B.W., 2012. Regulation of retinoblastoma protein (Rb) by p21 is critical for adaptation to massive small bowel resection. *J Gastrointest Surg* 16(1):148-155; discussion 155.
- [59] Gorgoulis, V., Adams, P.D., Alimonti, A., Bennett, D.C., Bischof, O., Bishop, C., et al., 2019. Cellular Senescence: Defining a Path Forward. *Cell* 179(4):813-827.
- [60] Park, E.J., Min, K.J., Lee, T.J., Yoo, Y.H., Kim, Y.S., Kwon, T.K., 2014. beta-Lapachone induces programmed necrosis through the RIP1-PARP-AIF-dependent pathway in human hepatocellular carcinoma SK-Hep1 cells. *Cell Death Dis* 5:e1230.
- [61] Hars, E.S., Lyu, Y.L., Lin, C.P., Liu, L.F., 2006. Role of apoptotic nuclease caspase-activated DNase in etoposide-induced treatment-related acute myelogenous leukemia. *Cancer Res* 66(18):8975-8979.
- [62] Perkins, C.L., Fang, G., Kim, C.N., Bhalla, K.N., 2000. The role of Apaf-1, caspase-9, and bid proteins in etoposide- or paclitaxel-induced mitochondrial events during apoptosis. *Cancer Res* 60(6):1645-1653.
- [63] Maas, C., de Vries, E., Tait, S.W., Borst, J., 2011. Bid can mediate a pro-apoptotic response to etoposide and ionizing radiation without cleavage in its unstructured loop and in the absence of p53. *Oncogene* 30(33):3636-3647.
- [64] Lallemand, Y., Luria, V., Haffner-Krausz, R., Lonai, P., 1998. Maternally expressed PGK-Cre transgene as a tool for early and uniform activation of the Cre site-specific recombinase. *Transgenic Res* 7(2):105-112.
- [65] Schiff, M., Benit, P., El-Khoury, R., Schlemmer, D., Benoist, J.F., Rustin, P., 2011. Mouse studies to shape clinical trials for mitochondrial diseases: high fat diet in Harlequin mice. *PLoS One* 6(12):e28823.
- [66] Vahsen, N., Cande, C., Briere, J., Benit, P., Rustin, P., Kroemer, G., 2004. The absence of apoptosis-inducing factor AIF induces complex I deficiency. *Biochim Biophys Acta* 1657:83.

- [67] Larsson, N.G., Wang, J., Wilhelmsson, H., Oldfors, A., Rustin, P., Lewandoski, M., et al., 1998. Mitochondrial transcription factor A is necessary for mtDNA maintenance and embryogenesis in mice. *Nat Genet* 18(3):231-236.
- [68] Humble, M.M., Young, M.J., Foley, J.F., Pandiri, A.R., Travlos, G.S., Copeland, W.C., 2013. *Polg2* is essential for mammalian embryogenesis and is required for mtDNA maintenance. *Hum Mol Genet* 22(5):1017-1025.
- [69] Yuste, V.J., Moubarak, R.S., Delettre, C., Bras, M., Sancho, P., Robert, N., et al., 2005. Cysteine protease inhibition prevents mitochondrial apoptosis-inducing factor (AIF) release. *Cell Death Differ* 12(11):1445-1448.
- [70] Wang, Y., Dawson, V.L., Dawson, T.M., 2009. Poly(ADP-ribose) signals to mitochondrial AIF: a key event in parthanatos. *Exp Neurol* 218(2):193-202.
- [71] Wang, H., Yu, S.W., Koh, D.W., Lew, J., Coombs, C., Bowers, W., et al., 2004. Apoptosis-inducing factor substitutes for caspase executioners in NMDA-triggered excitotoxic neuronal death. *J Neurosci* 24(48):10963-10973.
- [72] Cheung, E.C., Melanson-Drapeau, L., Cregan, S.P., Vanderluit, J.L., Ferguson, K.L., McIntosh, W.C., et al., 2005. Apoptosis-inducing factor is a key factor in neuronal cell death propagated by BAX-dependent and BAX-independent mechanisms. *J Neurosci* 25(6):1324-1334.
- [73] Ishihara, N., Takagi, N., Niimura, M., Takagi, K., Nakano, M., Tanonaka, K., et al., 2005. Inhibition of apoptosis-inducing factor translocation is involved in protective effects of hepatocyte growth factor against excitotoxic cell death in cultured hippocampal neurons. *J Neurochem* 95(5):1277-1286.
- [74] Zong, W.X., Ditsworth, D., Bauer, D.E., Wang, Z.Q., Thompson, C.B., 2004. Alkylating DNA damage stimulates a regulated form of necrotic cell death. *Genes Dev* 18(11):1272-1282.
- [75] Hegedus, C., Lakatos, P., Olah, G., Toth, B.I., Gergely, S., Szabo, E., et al., 2008. Protein kinase C protects from DNA damage-induced necrotic cell death by inhibiting poly(ADP-ribose) polymerase-1. *FEBS Lett* 582(12):1672-1678.
- [76] Wang, Y., Kim, N.S., Li, X., Greer, P.A., Koehler, R.C., Dawson, V.L., et al., 2009. Calpain activation is not required for AIF translocation in PARP-1-dependent cell death (parthanatos). *J Neurochem* 110(2):687-696.
- [77] Arnoult, D., Parone, P., Martinou, J.C., Antonsson, B., Estaquier, J., Ameisen, J.C., 2002. Mitochondrial release of apoptosis-inducing factor occurs downstream of cytochrome c release in response to several proapoptotic stimuli. *J Cell Biol* 159(6):923-929.
- [78] Munoz-Pinedo, C., Guio-Carrion, A., Goldstein, J.C., Fitzgerald, P., Newmeyer, D.D., Green, D.R., 2006. Different mitochondrial intermembrane space proteins are released during apoptosis in a manner that is coordinately initiated but can vary in duration. *Proc Natl Acad Sci U S A* 103(31):11573-11578.
- [79] Joza, N., Susin, S.A., Daugas, E., Stanford, W.L., Cho, S.K., Li, C.Y., et al., 2001. Essential role of the mitochondrial apoptosis-inducing factor in programmed cell death. *Nature* 410(6828):549-554.
- [80] Lyon, M.F., Rastan, S., 1984. Parental source of chromosome imprinting and its relevance for X chromosome inactivation. *Differentiation* 26(1):63-67.
- [81] Heard, E., 2004. Recent advances in X-chromosome inactivation. *Curr Opin Cell Biol* 16(3):247-255.
- [82] Krietsch, W.K., Fundele, R., Kuntz, G.W., Fehlau, M., Burki, K., Illmensee, K., 1982. The expression of X-linked phosphoglycerate kinase in the early mouse embryo. *Differentiation* 23(2):141-144.

- [83] Banerjee, H., Das, A., Srivastava, S., Mattoo, H.R., Thyagarajan, K., Khalsa, J.K., et al., 2012. A role for apoptosis-inducing factor in T cell development. *J Exp Med* 209(9):1641-1653.
- [84] Peng, X., Lin, Q., Liu, Y., Jin, Y., Druso, J.E., Antonyak, M.A., et al., 2013. Inactivation of Cdc42 in embryonic brain results in hydrocephalus with ependymal cell defects in mice. *Protein Cell* 4(3):231-242.
- [85] Appelbe, O.K., Bollman, B., Attarwala, A., Triebes, L.A., Muniz-Talavera, H., Curry, D.J., et al., 2013. Disruption of the mouse *Jhy* gene causes abnormal ciliary microtubule patterning and juvenile hydrocephalus. *Dev Biol* 382(1):172-185.
- [86] Wyss, L., Schafer, J., Liebner, S., Mittelbronn, M., Deutsch, U., Enzmann, G., et al., 2012. Junctional adhesion molecule (JAM)-C deficient C57BL/6 mice develop a severe hydrocephalus. *PLoS One* 7(9):e45619.
- [87] Park, R., Moon, U.Y., Park, J.Y., Hughes, L.J., Johnson, R.L., Cho, S.H., et al., 2016. Yap is required for ependymal integrity and is suppressed in LPA-induced hydrocephalus. *Nat Commun* 7:10329.
- [88] Cao, M., Wu, J.I., 2015. Camk2a-Cre-mediated conditional deletion of chromatin remodeler Brg1 causes perinatal hydrocephalus. *Neurosci Lett* 597:71-76.
- [89] Vogel, P., Read, R.W., Hansen, G.M., Payne, B.J., Small, D., Sands, A.T., et al., 2012. Congenital hydrocephalus in genetically engineered mice. *Vet Pathol* 49(1):166-181.
- [90] Parikh, S., Saneto, R., Falk, M.J., Anselm, I., Cohen, B.H., Haas, R., et al., 2009. A modern approach to the treatment of mitochondrial disease. *Curr Treat Options Neurol* 11(6):414-430.
- [91] Olsen, R.K., Olpin, S.E., Andresen, B.S., Miedzybrodzka, Z.H., Pourfarzam, M., Merinero, B., et al., 2007. ETFDH mutations as a major cause of riboflavin-responsive multiple acyl-CoA dehydrogenation deficiency. *Brain* 130(Pt 8):2045-2054.
- [92] Avula, S., Parikh, S., Demarest, S., Kurz, J., Gropman, A., 2014. Treatment of mitochondrial disorders. *Curr Treat Options Neurol* 16(6):292.

**Figure 1. AIF loss led to ETC dysfunction and mitochondrial network disorganization.** (A) To generate  $AIF^{-/Y}$  MEFs, we crossed the Rosa26-CreERT2 mice with the *Aifm1* floxed strain [35]. Among the embryos, E12.5  $AIF^{Fl/Y}; RosaCre ERT2^{+/-}$  embryos were genetically identified and dissected. After MEFs generation and expansion, cells were treated overnight with tamoxifen (4-OHT; 1 $\mu$ M) to induce *Aifm1* exon 11 excision [35]. (B) Representative time-course immunoblot of untreated (0) or 4-OHT-treated MEFs (1 to 18 days post-treatment) revealing the progressive loss of AIF and key proteins of the ETC complexes I and IV. Equal loading was confirmed by  $\beta$ -Actin probing. This experiment was repeated three times with similar results. (C) Multi-protein complex assessment by blue native polyacrylamide gel electrophoresis (BN-PAGE) in mitochondria purified from control (0) or 4-OHT-treated MEFs (4 to 16 days post-addition). *Up to down gel pictures*: (i) Mitochondrial complex I and complex I-containing supercomplexes visualized by immunoblot (NDUFA9); (ii) Representative result of a NADH dehydrogenase complex I in-gel test revealing ETC supercomplex disorganization after AIF loss; (iii) and (iv) Complex III dimer (UQCRC2) and IV monomer (COX4I2) detected by immunoblot. This experiment was repeated five times with similar results. (D) Analysis of the mitochondrial network changes associated to AIF loss. *Upper panels*, representative immunofluorescence images of control (D0) and  $AIF^{-/Y}$  MEFs (D12 and D16) labeled with Mitotracker Red (mitochondria) and Hoechst (nucleus). Bar: 100  $\mu$ m. *Lower panels*, control (D0) and  $AIF^{-/Y}$  MEFs (D12 and D16) analyzed by electron microscopy. Representative microphotographs are shown. Black squares underline mitochondrial features. Bar: 0.5  $\mu$ m. (E) Mitofusin 1 (Mfn1), mitofusin 2 (Mfn2), mitochondrial dynamin like GTPase (Opa1), mitochondrial fission 1 protein (Fis1), dynamin-related protein 1 (Dnm1l), and mitochondrial fission factor (Mff) mRNA levels determined by quantitative RT-PCR in control (D0) and  $AIF^{-/Y}$  MEFs (D12) (n = 4). 18S mRNA expression was used to normalize data. Results are expressed as a ratio of mRNA expression relative to control (D0) cells (set at 1.0). (F) Flow cytometry  $\Delta\Psi_m$  assessment performed by Mitotracker Red labeling in control (D0) and  $AIF^{-/Y}$  MEFs (D16) and expressed as a plot (n = 8). Data were obtained in 10,000 cells and expressed as mean fluorescence intensity (MFI). (G) Mitochondrial ROS levels recorded in control (D0) and  $AIF^{-/Y}$  MEFs (D16) and graphed (n = 9). Data were obtained in 10,000 cells and expressed as mean fluorescence intensity (MFI). (H) Sod1 and Sod2 mRNA levels determined by quantitative RT-PCR in control (D0) and  $AIF^{-/Y}$  MEFs (D16) (n = 5). 18S mRNA expression was used to normalize data. Results are expressed as a ratio of mRNA expression relative to control (D0) cells (set at 1.0). (I) ATP/ADP ratio recorded in control (D0) and  $AIF^{-/Y}$  MEFs (D16) left untreated or pre-treated with oligomycin (10  $\mu$ M) (n = 7). Results are expressed as a ratio of ATP/ADP relative to control (D0) cells



(considered as a 100 %). Statistical significance was calculated by Mann Whitney (**E, H**) or student *t* (**F, G, I**) tests. Bars represent mean  $\pm$  SEM.

**Figure 2. Mitochondrial OXPHOS dysfunction was counterbalanced in *AIF*<sup>-/-</sup> MEFs by a shift towards anaerobic glycolysis and the development of a senescent phenotype.** (**A**) Kinetic phosphorylation of AMPK visualized by immunoblot in left untreated (0) or 4-OHT-treated MEFs (4 to 16 days post-treatment). Equal loading was confirmed by  $\beta$ -Actin probing. This experiment was repeated three times with similar results. (**B**) Glut-1 and Glut-4 mRNA levels determined by quantitative RT-PCR in control (D0) and *AIF*<sup>-/-</sup> MEFs (D12 and D16) (n = 8). 18S mRNA expression was used to normalize data. Results are expressed as a ratio of mRNA expression relative to control (D0) cells (set at 1.0). (**C**) Glucose uptake measured by the assimilation of 2-NBDG in control (D0) and *AIF*<sup>-/-</sup> MEFs (D12 and D16) untreated or pre-treated with indinavir (50 $\mu$ M) (n = 6). Results are expressed as a ratio relative to control (D0) cells (set at 1.0). (**D**) Lactate release recorded in control (D0) and *AIF*<sup>-/-</sup> MEFs (D12 and D16) as described in the Methods section (n = 4). (**E**) Cytofluorometric assessment of cell death performed in control (D0) and *AIF*<sup>-/-</sup> MEFs (D12 and D16) untreated or pre-treated with indinavir (50  $\mu$ M) and labeled with AnnexinV and PI. The frequency of positive staining, which represents dying cells, was recorded and expressed as a plot (n = 6). (**F**) Flow cytometry cell cycle analysis performed in control (D0) and *AIF*<sup>-/-</sup> MEFs (D12 and D16) by BrdU and PI (DNA content) co-labeling. *Left*, Representative cytometric panels of control (D0) and *AIF*<sup>-/-</sup> MEFs (D16). *Right*, the % of cells in phase S was quantified and expressed as a plot (n = 4). (**G**) Cytometric evaluation of senescence in control (D0) and *AIF*<sup>-/-</sup> MEFs (D12 and D16) using the  $\beta$ -galactosidase substrate C12FDG. Representative flow cytometric profiles of control (D0) and *AIF*<sup>-/-</sup> MEFs (D16). (**H**) The percentage of C12FDG positive control (D0) and *AIF*<sup>-/-</sup> MEFs (D12 and D16) measured as in (**G**) was calculated and graphed (n = 4). (**I**) Tp53 mRNA levels determined by qPCR in control (D0) and *AIF*<sup>-/-</sup> MEFs (D12 and D16) (n = 5). 18S mRNA expression was used to normalize data. Results are expressed as a ratio of mRNA expression relative to control (D0) cells (set at 1.0). (**J**) *Left*, Cdkn1 $\alpha$  mRNA levels determined by qPCR in control (D0) and *AIF*<sup>-/-</sup> MEFs (D12 and D16) (n = 6). 18S mRNA expression was used to normalize data. Results are expressed as a ratio of mRNA expression relative to control (D0) cells (set at 1.0). *Right*, representative immunoblot of control (D0) and *AIF*<sup>-/-</sup> MEFs (D12 and D16) revealing the cell cycle inhibitor P21. Equal loading was confirmed by  $\beta$ -Actin probing (n = 4 experiments with similar results). (**K**) Representative immunoblot of control (D0) and *AIF*<sup>-/-</sup> MEFs (D12 and D16) revealing the decrease in pRb phosphorylation (P-pRb) associated to AIF loss. Equal loading was confirmed by  $\beta$ -Actin probing (n = 3 experiments with similar results).

Statistical significance was calculated by Mann Whitney (**D, F, H, I**) or student *t* (**B, C, E, J**) tests. Bars represent mean  $\pm$  SEM.

**Figure 3. Lentiviral transduction of  $AIF^{-/Y}$  MEFs with V5 tagged AIF-wt cDNA restored a normal mitochondrial OXPHOS/metabolism and corroborated the specific role of AIF in MNNG- and  $\beta$ -Lapachone-mediated cell death.** (A) Representative confocal images of  $AIF^{+/Y}$  (WT),  $AIF^{-/Y}$  (AIF KO), and  $AIF^{-/Y}$  expressing AIF-wt MEFs (AIF KO + AIF-V5) labeled with MitoTrackerRed (mitochondria) and Hoechst (nucleus) corroborating that lentiviral transduced AIF-V5 relocalized into mitochondria and reconstituted the mitochondrial network. Bar: 100  $\mu$ m. (B) Representative immunoblot of the panel of MEFs used in (A) showing the presence of AIF and key proteins of the ETC complexes I to V after the lentiviral transduction of AIF-V5 into the  $AIF^{-/Y}$  MEFs. Equal loading was confirmed by  $\beta$ -Actin. This experiment was repeated five times with similar results. (C) Mitochondrial supercomplex picturing of WT, AIF KO, and AIF KO + AIF-V5 performed by 1D BN-PAGE as in Figure 1C. Mitochondrial supercomplexes and complex I were detected by NDUFA9 immunoblotting, complex III (dimer) was visualized by UQCRC2 blotting. This experiment was repeated three times with similar results. (D) Assessment of basal (coupled) and maximal respiration (uncoupled) in WT, AIF KO, and AIF KO + AIF-V5 MEFs using a Clark's electrode. Basal respiration corresponds to O<sub>2</sub> consumption rate coupled to ATP production, whereas sequential addition of 10  $\mu$ M oligomycin (ATP synthase inhibitor), 15  $\mu$ M fluoro-carbonyl cyanide phenylhydrazone (FCCP; uncoupling agent measuring the maximal respiration capacity), 2 mM amytal (complex I inhibitor) or 5mM sodium azide (mitochondrial OXPHOS inhibitor) enable calculation of the maximal oxygen consumption rate. The % of activity (relative to that measured in WT cells -considered as a 100 %-) in coupled and uncoupled conditions was expressed as a histogram (n = 5 independent experiments). Note that the lentiviral transduction of AIF-V5 into the AIF KO MEFs fully restored mitochondrial respiration. (E) Glucose uptake measured by assimilation of 2-NBDG in WT, AIF KO, and AIF KO + AIF-V5 MEFs (n = 4). Results are expressed as a ratio of mRNA expression relative to control (D0) cells (set at 1.0). (F) Lactate release recorded in WT, AIF KO, and AIF KO + AIF-V5 MEFs as described in the Methods section (n = 4). (G) The panel of MEFs used in (A) to (F) were untreated or treated with 2-Deoxy-D-Glucose (2-DG; 10 mM; 24 h) and labeled with AnnexinV and PI. The frequency of positive staining, which represents dying cells, was recorded and expressed as a plot (n = 4). (H) The panel of MEFs used in (A) to (F) were untreated or treated with *N*-methyl-*N'*-nitro-*N'*-nitrosoguanidine (MNNG) (250 mM; 9 h), staurosporine (STS; 1  $\mu$ M; 6 h),  $\beta$ -Lapachone (4  $\mu$ M; 18 h), or etoposide (20  $\mu$ M; 6 h) in the absence or presence of the broad caspase-inhibitor QVD.OPh (1  $\mu$ M). Then, MEFs were labeled with AnnexinV and PI and the frequency of positive staining, which represents

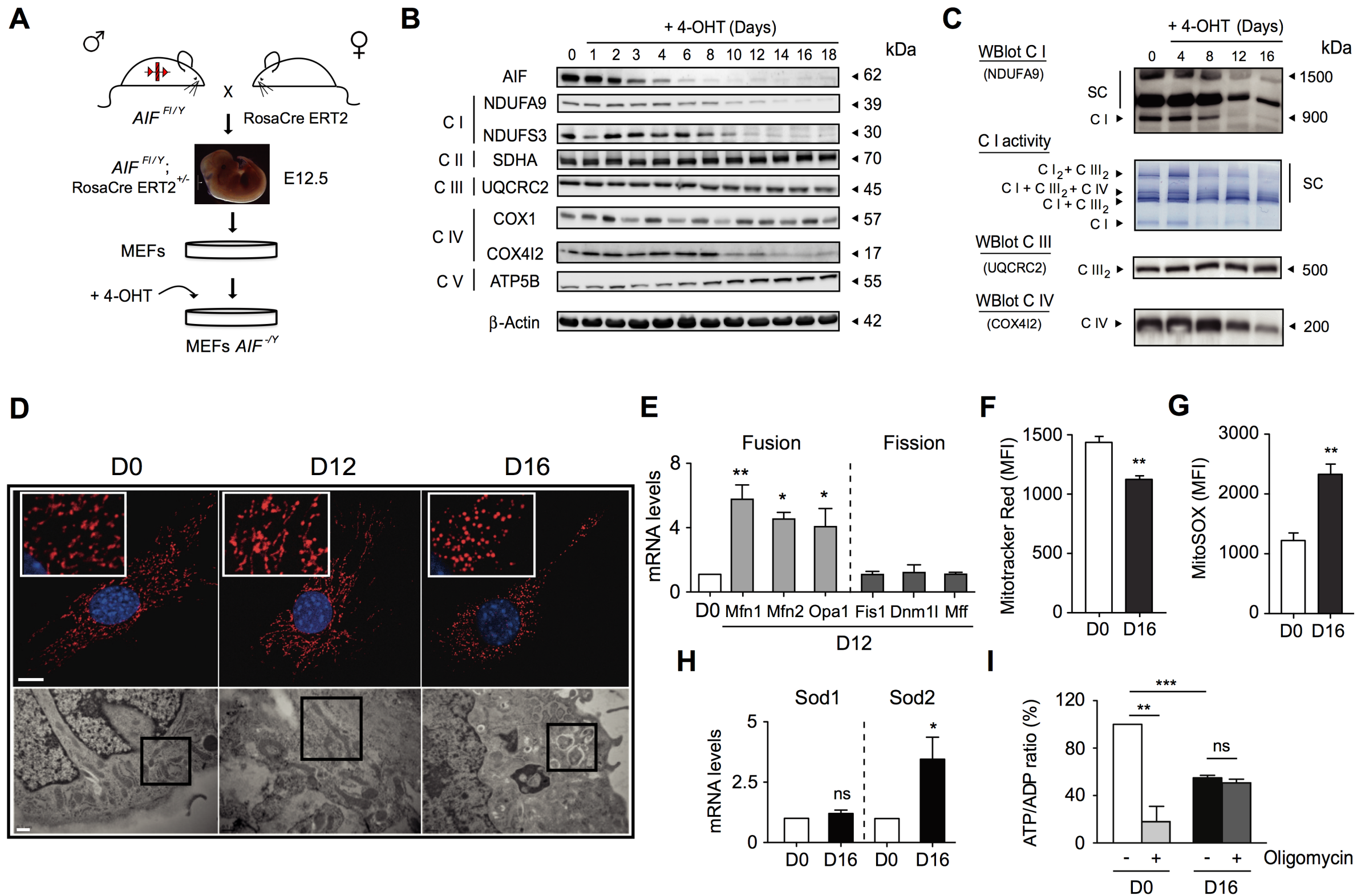
dying cells, was recorded and graphed ( $n = 6$ ). Statistical significance was calculated by Mann Whitney (**D, E, F, G**) or student  $t$  (**H**) tests. Bars represent mean  $\pm$  SEM.

**Figure 4. A significant percentage of  $AIF^{+/-}$  females developed a hydrocephalus phenotype associated to developmental defaults and an excess of mitochondrial ROS.** (**A**) To generate  $AIF^{+/-}$  animals, we crossed *Aifm1* floxed males with PGK-Cre females. The table below indicates the offspring distribution. About 10 % of  $AIF^{+/-}$  females developed a hydrocephalus (HC) phenotype. Photographs depict the phenotype of a 2.5 week-old  $AIF^{+/-}$  HC female and a HC brain compared to a WT brain. Note the swelling of the cranial cavity of the mice and the excess of cerebrospinal fluid (CSF) that warps the HC brain. (**B**) Representative hematoxylin/eosin (HE) labeled sections of 2.5 week-old WT and  $AIF^{+/-}$  HC females showing (left to right): sagittal sections (entire mice and head) and coronal sections (brain and cerebellum). Note the extension of the hydrocephaly, the brain compression exerted by the CSF excess, and the herniated cerebellum in the  $AIF^{+/-}$  HC. (**C**) HE stained brain sections from 2.5 week-old  $AIF^{+/-}$  HC animals showing spinal and parenchymatous haemorrhages and loss and defects of ciliation in the ependymal epithelium. Bar: 50  $\mu$ m. (**D**) Oxidative modification of proteins assessed by carbonylation immunoblot on brain homogenates from 2.5 week-old WT,  $AIF^{+/-}$ , and  $AIF^{+/-}$  HC mice. This experiment was repeated three times with similar results. The OD ratio depicted in the graph illustrates the levels of protein carbonylation of the different phenotypes. Results are expressed as a ratio of OD relative to WT cells (set at 1.0). (**E**) PGK-Cre dams were supplied or not with riboflavin in drinking water (5 mg/L) and the number and genotype/phenotype of the progeny were assessed and reported in a table. (**F**) Characteristic immunofluorescence images of brains from 2.5 week-old WT,  $AIF^{+/-}$  HC and  $AIF^{+/-}$  mice supplied with riboflavin ( $AIF^{+/-}$  + Rb) showing the microglial (Iba1 labeling) status. Individual cells were visualized by Hoechst (nuclear) co-staining. Bar: 200  $\mu$ m. Statistical significance in (**D**) was calculated by Mann Whitney test. Bars represent mean  $\pm$  SEM.

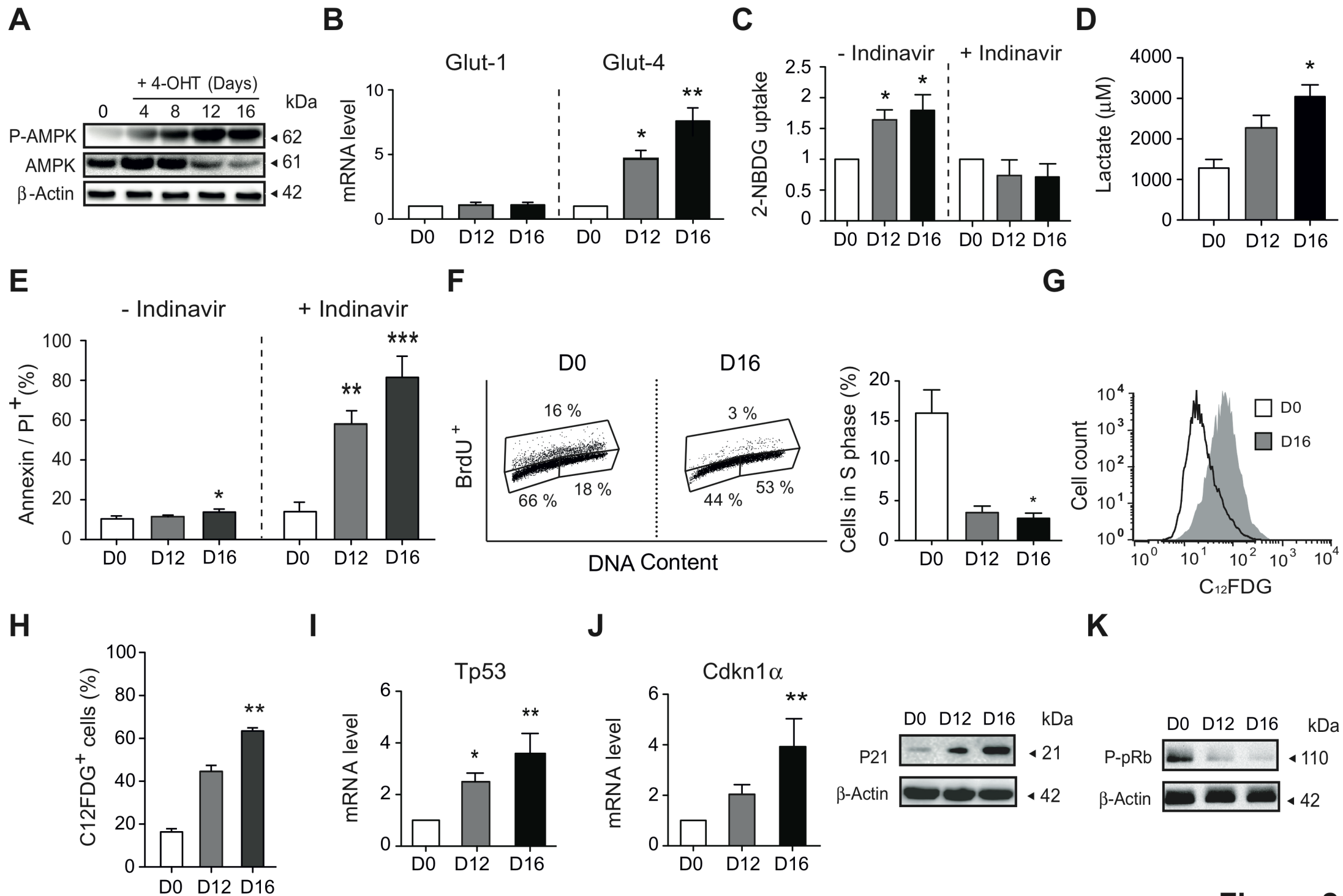
**Figure 5. Mitochondrial AIF deficiency induced murine embryonic lethality linked to OXPHOS deficiency and energy loss.** (**A**) To generate AIF KO mice, we crossed  $AIF^{+/-}$  females with C57BL/6 WT males. After genetic identification, the result of the crossing (progeny and E8.5 to E13.5 embryos) was reported in a table. (**B**) Light microscope images of E7.5 to E9.5  $AIF^{+/Y}$  and  $AIF^{-/Y}$  embryos illustrating the progressive growth delay of the AIF KO embryos. Bar: 500  $\mu$ m. (**C**) Hematoxylin/eosin staining performed in sagittal sections of E8.5 and E9.5  $AIF^{+/Y}$  and  $AIF^{-/Y}$  embryos underlining the morphology and the abnormal nervous development of the AIF KO embryos. Bar: 500  $\mu$ m. (**D**) Electron microscopy picturing mitochondria of E9.5  $AIF^{+/Y}$  and  $AIF^{-/Y}$  embryos. Representative microphotographs are shown. Arrowheads in the picture mark the mitochondria. White squares show characteristic mitochondria. Bar: 0.5  $\mu$ m. (**E**) Immunoblot of

AIF and key proteins of the ETC complexes I to V performed in whole protein extracts from E9.5  $AIF^{+/Y}$  and  $AIF^{-/Y}$  embryos. Equal loading was confirmed by  $\beta$ -Actin probing. This experiment was repeated four times with similar results. **(F)** Representative results of the histochemical assessment of mitochondrial OXPHOS activity in E9.5  $AIF^{+/Y}$  and  $AIF^{-/Y}$  embryos using cytochrome c oxidase/succinate dehydrogenase (COX/SDH) double-labeling. Bar: 50  $\mu$ m. Whereas OXPHOS activity is normal in  $AIF^{+/Y}$  embryos, as demonstrated by the brown color of the section,  $AIF^{-/Y}$  showed defective OXPHOS activity (absence of brown staining). This experiment was repeated three times with similar results. **(G)** Total ATP levels recorded, as described in Methods section, in E9.5  $AIF^{+/Y}$  and  $AIF^{-/Y}$  embryos (n = 6). Results are expressed as RLU (relative light units). **(H)** Lactate release measured, as described in Methods section, in E9.5  $AIF^{+/Y}$  and  $AIF^{-/Y}$  embryos (n = 6). Statistical significance in **(G)** and **(H)** was calculated by the student *t* test. Bars represent mean  $\pm$  SEM.

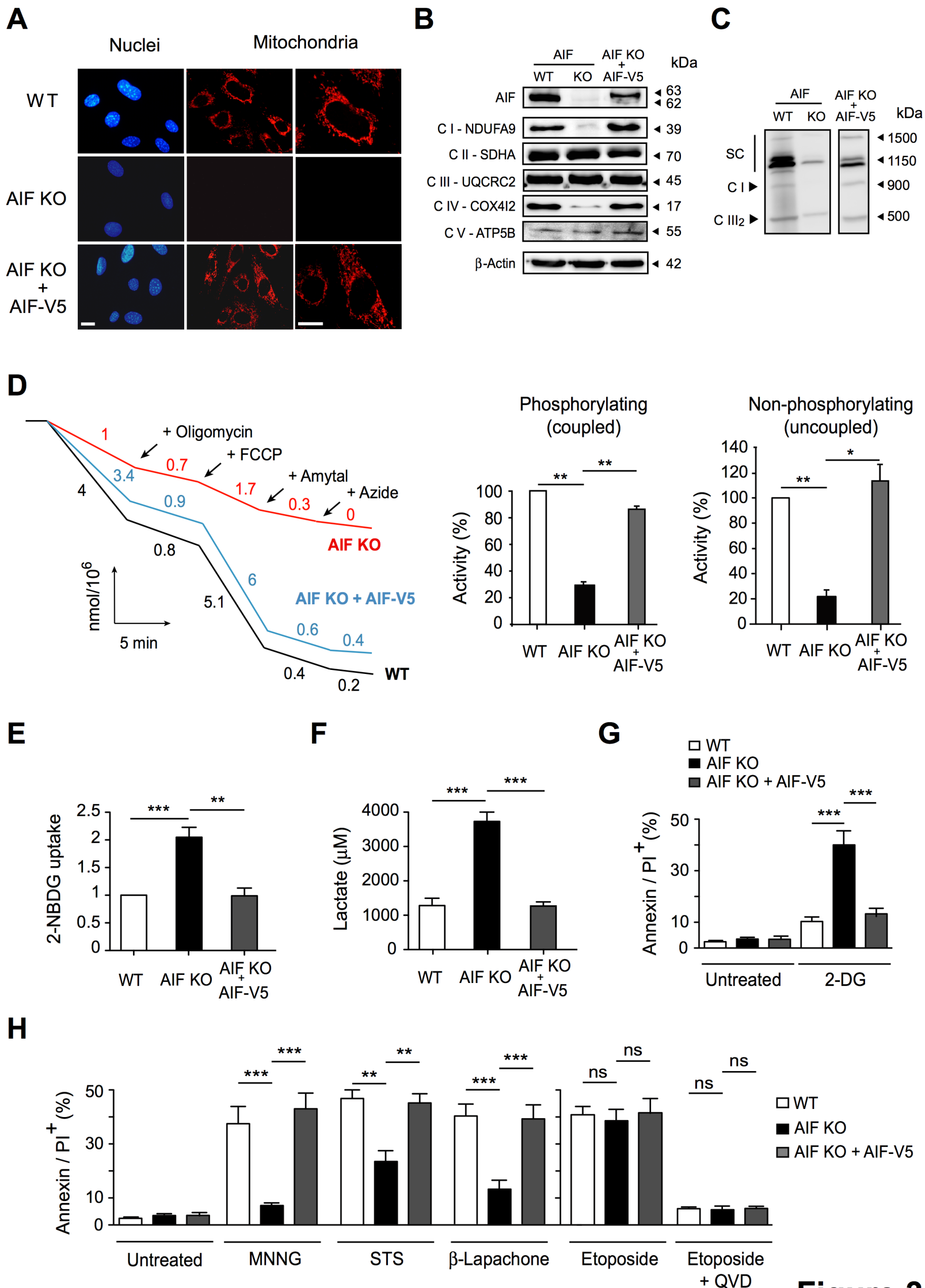
**Figure 6. Embryonic AIF loss triggered arrest of proliferation and enhancement of cellular apoptotic levels.** **(A)** BrdU immunofluorescence analysis of frozen section of  $AIF^{+/Y}$  and  $AIF^{-/Y}$  embryos at E8.5 and E9.5. Photographs visualized the head of a representative embryo. Bar: 500  $\mu$ m. The BrdU labeling index was calculated as the ratio of BrdU/Hoechst fluorescence measured in a fixed surface. Data in the histogram represent mean  $\pm$  SEM (n = ratio obtained in at least 5 different surfaces of 3 independent embryonic sections). **(B)** TUNEL staining of PFA fixed cryosection of  $AIF^{+/Y}$  and  $AIF^{-/Y}$  embryos at E8.5 and E9.5. Bar: 500  $\mu$ m. The TUNEL labeling index was obtained as the ratio of TUNEL/Hoechst fluorescence measured in a fixed surface. Data in the histogram represent mean  $\pm$  SEM (n = ratio obtained in at least 5 different surfaces of 3 independent embryonic sections). Statistical significance in **(A)** and **(B)** was calculated by the student *t* test. Bars represent mean  $\pm$  SEM.



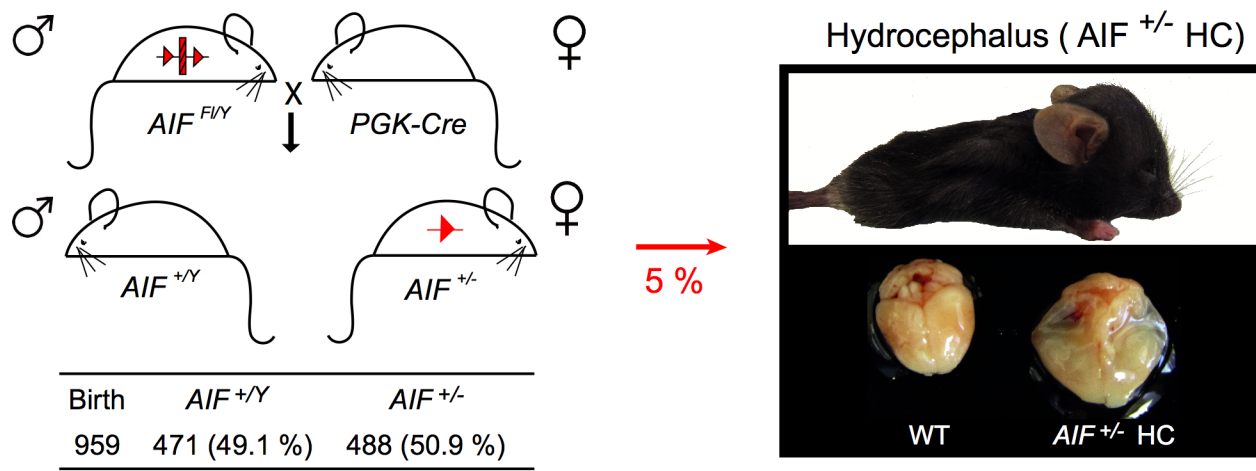
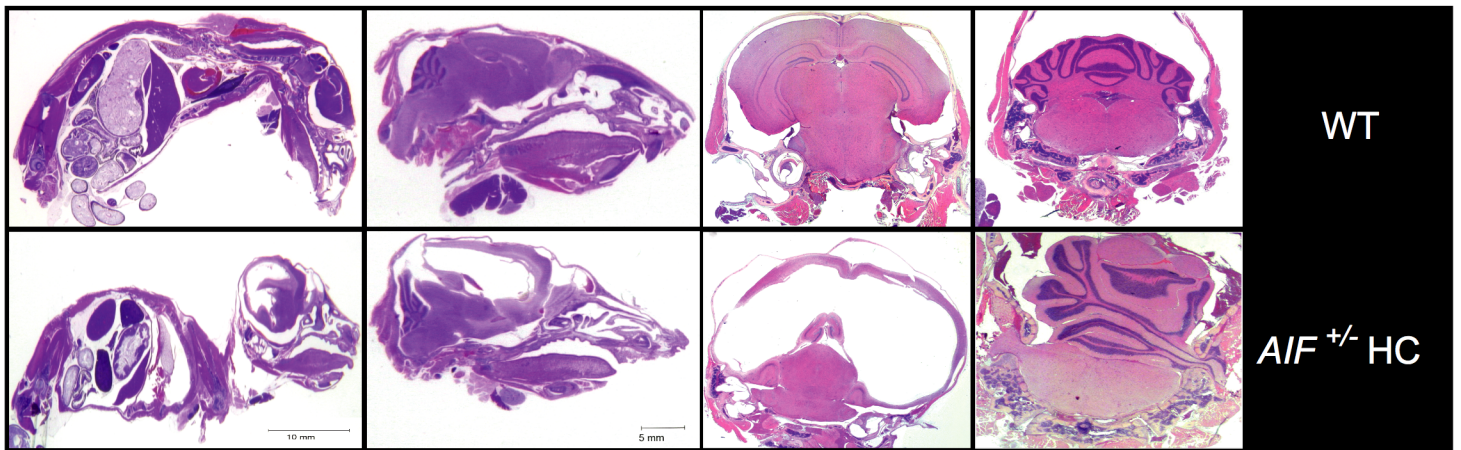
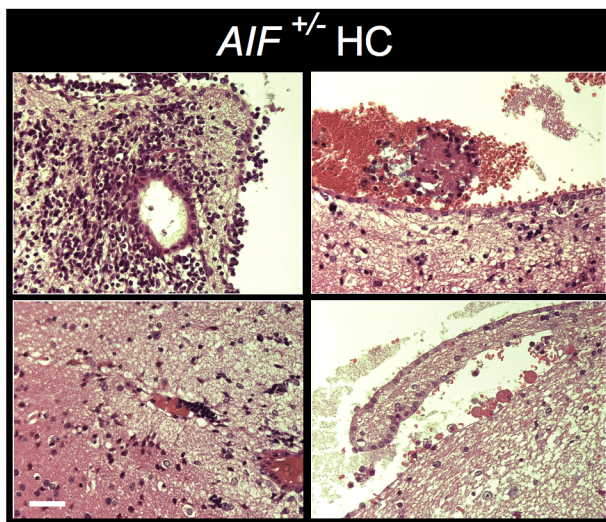
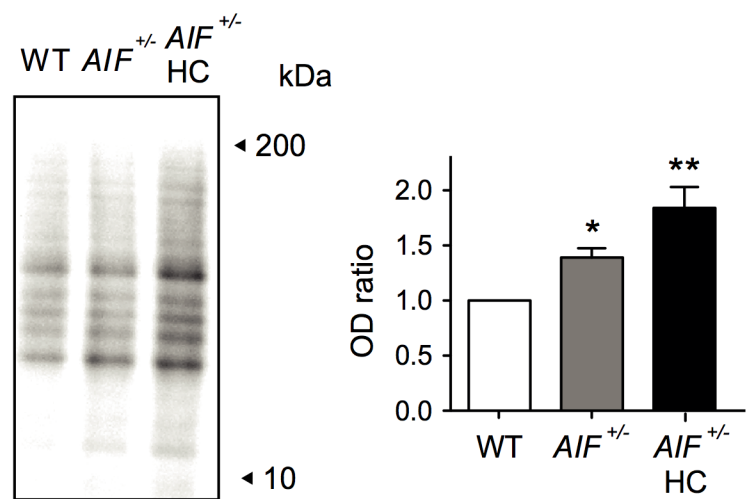
**Figure 1**



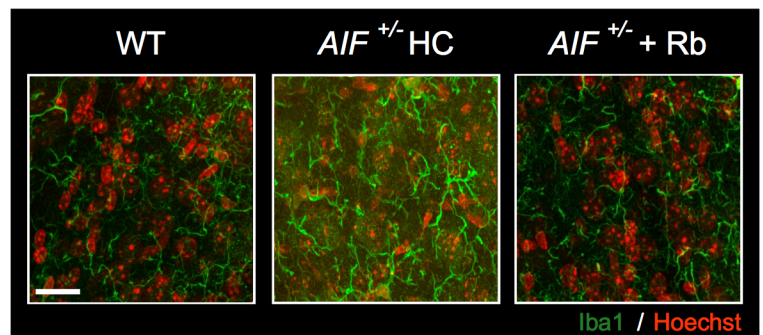
**Figure 2**



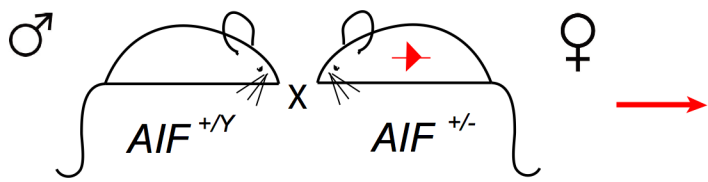
**Figure 3**

**A****B****C****D****E**

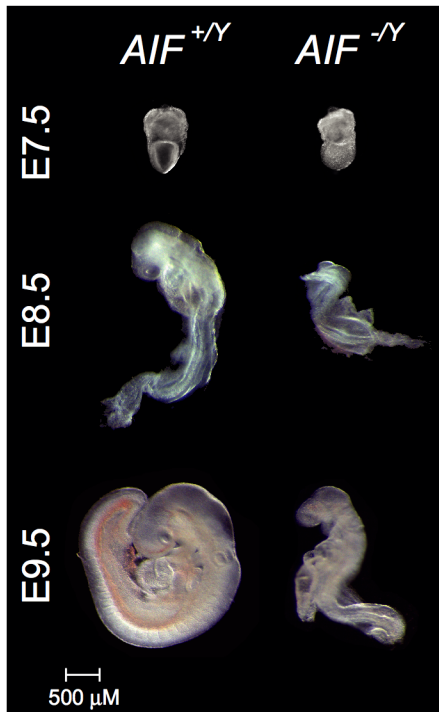
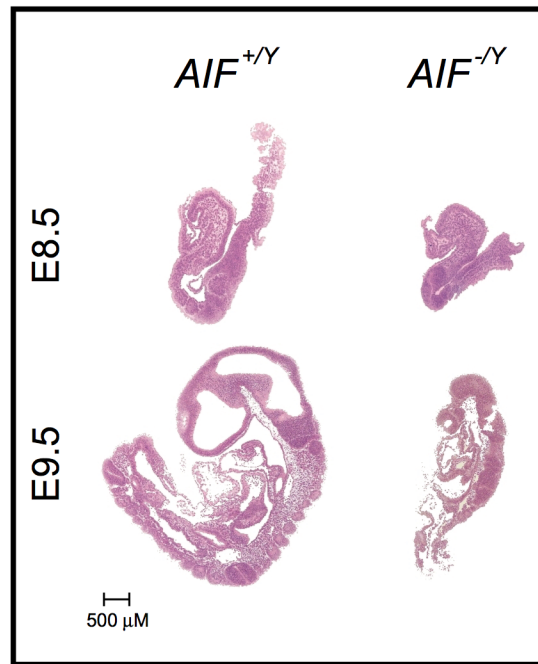
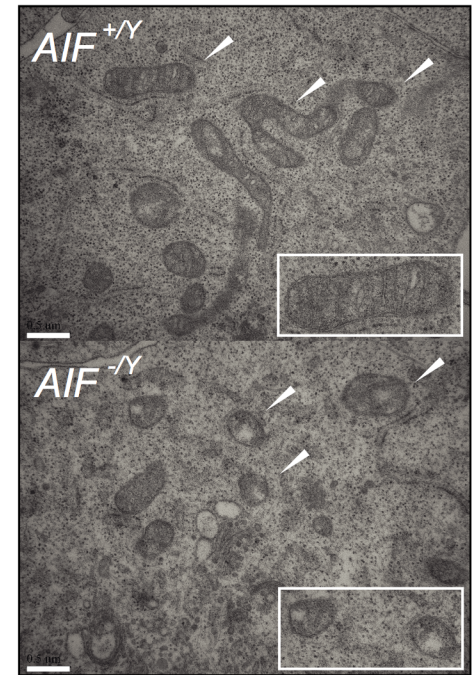
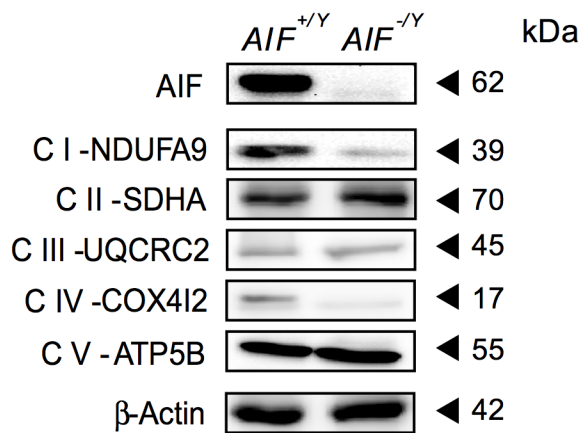
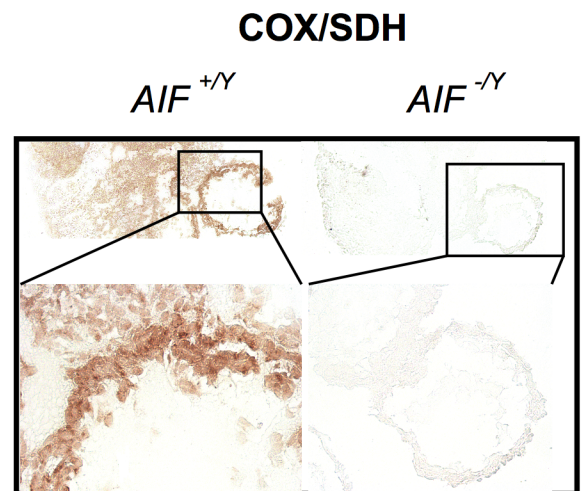
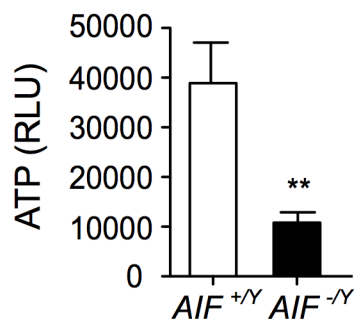
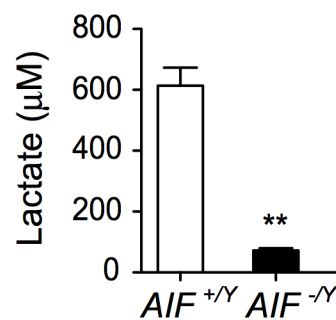
	AIF <sup>F1/Y</sup> ♂	X	PGK-Cre ♀
	- Riboflavin		+ Riboflavin
Birth	201		194
AIF <sup>+/Y</sup>	99 (49.2 %)		98 (50.5 %)
AIF <sup>+/-</sup>	92 (45.8 %)		94 (48.5 %)
AIF <sup>+/-</sup> HC	10 (5 %)		2 (1 %)

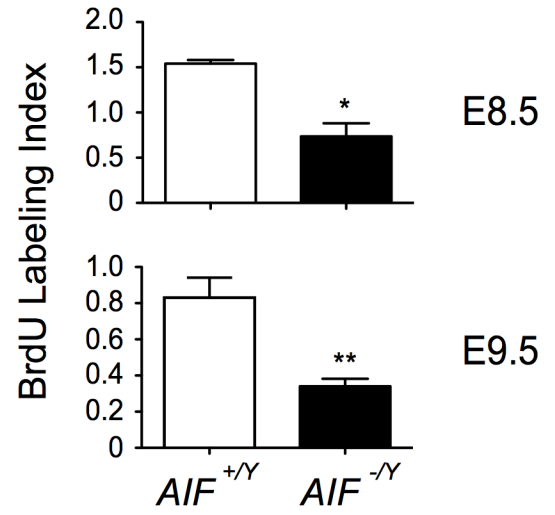
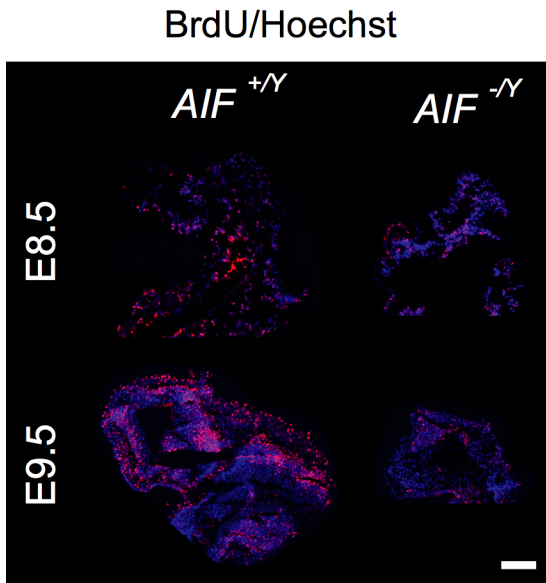
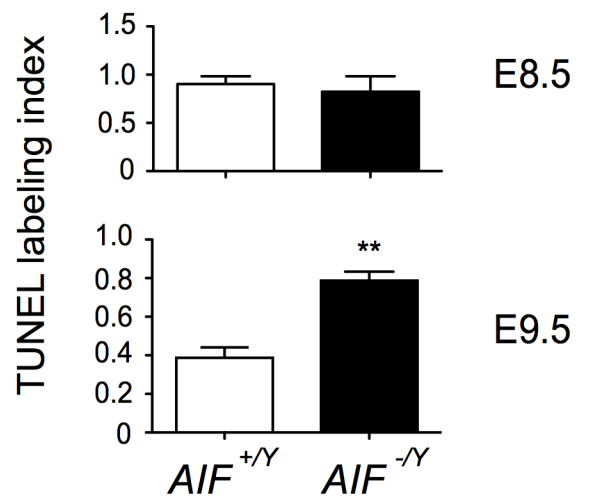
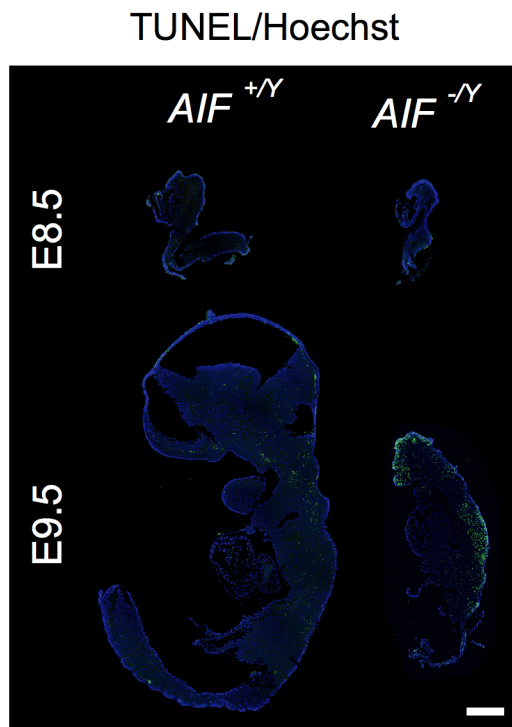
**F****Figure 4**



**A**

Stage	Total	+/+ & +/Y	+/-	-/Y
E8.5	35	10 (30 %)	14 (41 %)	11 (32 %)
E9.5	36	14 (39 %)	10 (28 %)	12 (33 %)
E10.5	39	13 (33 %)	16 (41 %)	10 (26 %)
E11.5	34	20 (59 %)	14 (41 %)	0 (0 %)
E13.5	31	27 (87%)	4 (13 %)	0 (0 %)
Birth	40	40 (100 %)	0 (0 %)	0 (0 %)

**B****C****D****E****F****G****H****Figure 5**

**A****B****Figure 6**

# Mitochondrial AIF loss causes metabolic reprogramming, caspase-independent cell death blockade, embryonic lethality, and perinatal hydrocephalus

Laure Delavallée et al.

-----

## Highlights

Mitochondrial AIF loss triggers OXPHOS/metabolism impairment

*AIF*<sup>-/-</sup> MEFs reprogram their metabolism by enabling an AMPK/GLUT-4 glycolytic pathway

The OXPHOS dysfunction associated to AIF loss generates a P53/P21 senescent phenotype

The lack of metabolic plasticity provokes embryonic lethality in the AIF KO animals

*AIF*<sup>+/-</sup> females develop immune cell exhaustion and perinatal hydrocephaly

**Mitochondrial AIF loss causes metabolic reprogramming,  
caspase-independent cell death blockade, embryonic  
lethality, and perinatal hydrocephalus**

**Laure Delavallée et al.**

-----

**CONFLICT OF INTEREST**

The authors declare no conflict of interest.